J. Fluid Mech. (2025), *vol.* 1019, A12, doi:10.1017/jfm.2025.10599

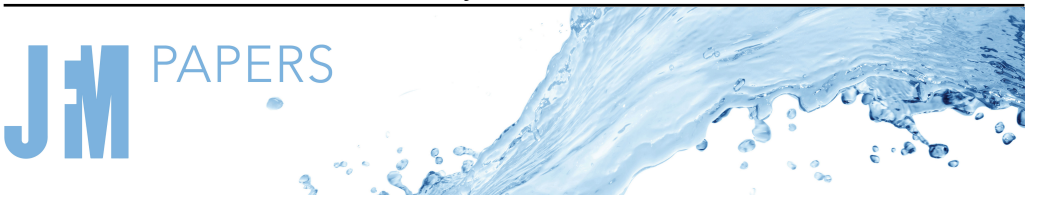

Development of smooth- and rough-wall boundary layers with strong sink flow favourable pressure gradients

Ralph J. Volino[1] **and Michael Paul Schultz**[2]

[1]Mechanical and Nuclear Engineering Department, United States Naval Academy, Annapolis, MD 21402, USA

[2]Naval Architecture and Ocean Engineering Department, United States Naval Academy, Annapolis, MD 21402, USA

Corresponding author: Ralph J. Volino, volino@usna.edu

(Received 16 April 2025; revised 8 July 2025; accepted 14 August 2025)

Sink flow boundary layers on smooth and rough walls were studied experimentally. In all cases a turbulent, zero-pressure-gradient boundary layer was subject to acceleration with $K = 3.2 \times 10^{-6}$, which suppressed the turbulence in the outer region and produced conditions similar to those in turbulent sink flow cases with lower K. In the smooth-wall case, after the momentum thickness Reynolds number had dropped to about 600, the near-wall turbulence then dropped, resulting in relaminarisation. In the rough-wall cases, the near-wall turbulence was sustained in spite of the strong favourable pressure gradient, and relaminarisation did not occur. A temporary equilibrium appears to occur that is similar to that seen with lower K, in spite of the ratio of the boundary-layer thickness to the roughness height dropping to less than 5. Mean velocity and Reynolds stress profiles, quadrant analysis and turbulence spectra are used to show the development of the boundary layer in response to the pressure gradient and the differences between the rough- and smooth-wall cases. This is believed to be the first study to consider the spatial evolution of constant-K rough-wall boundary layers with K large enough to cause relaminarisation in the smooth-wall case.

Key words: turbulent boundary layers, boundary layer structure

1. Introduction

Favourable pressure gradients (FPGs) can have a strong effect on turbulent boundary layers, and are seen in practice in numerous applications. Some examples include the

leading regions of airfoil surfaces and the hulls of marine vessels. An FPG increases velocity in the streamwise direction and reduces the boundary-layer thickness, resulting in increasing shear. The increasing shear can, however, be mitigated or even reversed by a second effect. An FPG is stabilising, and tends to reduce the turbulence in a boundary layer. If the FPG is strong enough and sustained for sufficient distance, a boundary layer can relaminarise. Reduced turbulent mixing tends to reduce skin friction. Many studies have considered FPG boundary layers on smooth walls. Narasimha & Sreenivasan (1973), for example, considered the mechanisms by which relaminarisation occurs. Narasimha & Sreenivasan (1979) and Sreenivasan (1982) provided discussions and reviews of relaminarisation.

An interesting type of FPG boundary layer is the sink flow that develops when the acceleration parameter, K, is held constant:

$$K = \frac{\nu}{U_e^2}\frac{\mathrm{d}U_e}{\mathrm{d}x}, \tag{1.1}$$

where ν is the kinematic viscosity, U_e is the local free-stream velocity and x is the streamwise coordinate. In the limit of zero boundary-layer thickness, a constant K is produced in the flow between two converging flat plates. A close approximation to a constant K also occurs in real boundary-layer flow between converging flat plates because the FPG keeps the boundary layers thin. If a sink flow could be continued for a sufficient streamwise distance, a singularity would be reached where the converging plates would meet, and the velocity would go to infinity. This distance is

$$x_{sink} = x - x_o = \frac{\nu}{KU_{eo}}, \tag{1.2}$$

where x_o and U_{eo} are taken at some upstream location, e.g. the start of the FPG. A sink flow boundary layer on a smooth wall will approach complete equilibrium, meaning that all dimensionless quantities reach asymptotic values and stop changing with x. This includes Reynolds numbers of all types, the skin friction coefficient and profiles of mean velocity and turbulence quantities expressed in inner or outer coordinates.

For a laminar boundary layer, the sink flow has an exact, closed-form solution, obtained by Pohlhausen (1921) and presented by Schlichting (1968). The turbulent, smooth-wall case has been considered in several studies, both experimentally and numerically. Jones & Launder (1972), for example, conducted experiments with K values between 1.5×10^{-6} and 3×10^{-6}. Spalart (1986) performed direct numerical simulations (DNS) for the same range of K. The studies found that relaminarisation occurred for K larger than about 3×10^{-6}. In cases where the boundary layer relaminarised, it was noted that the flow became 'quasi-laminar' as described by Narasimha & Sreenivasan (1973). Turbulent fluctuations remained in the boundary layer, but their dimensional magnitude remained approximately constant even as the flow accelerated. Similar behaviour has been noted in several studies (e.g. Blackwelder & Kovasznay 1972). Escudier *et al.* (1998) noted that the frequencies associated with the fluctuating velocities also remained constant instead of scaling with the increasing free-stream velocity. Narasimha & Sreenivasan (1973) referred to this fixed dimensional magnitude as 'frozen' turbulence, and 'frozen' is used to refer to this behaviour below. Piomelli & Yuan (2013) also noted that the streamwise Reynolds stress remained frozen at upstream values. They saw that the decrease of wall-normal and spanwise fluctuations was the main cause of inner-layer stabilisation, and that there were few ejections from the inner layer to the outer layer. As the fluctuations became increasingly small relative to the free-stream velocity, the mean flow approached a quasi-laminar state. While the turbulent fluctuations remain, their structure can change.

Bourassa & Thomas (2009) used quadrant analysis to show that an FPG reduces sweeps of high-speed fluid towards the wall relative to ejections of low-speed fluid moving away from the wall. They also noted an aliasing of quadrant-four events into quadrant three due to the streamwise pressure gradient, and found that this reduced the near-wall Reynolds shear stress.

At lower K the boundary layer remains turbulent with $KRe_\theta \approx 0.001$, and skin friction coefficient, $C_f = 2u_\tau^2/U_e{}^2 \approx 0.005$, where u_τ is the friction velocity and θ is the momentum thickness. The Clauser pressure gradient parameter, $\beta = Re_{\delta^*} K/(C_f/2) \approx -0.6$, where δ^* is the displacement thickness. These values appear to hold regardless of the K value. There is not a gradual change from the equilibrium turbulent condition to the laminar as K increases. Although turbulent, the Reynolds stresses are greatly reduced below those in a canonical zero-pressure-gradient (ZPG) boundary layer. Spalart (1986) noted that turbulent near-wall streaks remained, but that patches of non-turbulent flow were present in the instantaneous flow field. Other studies have reported similar results. Castillo & George (2001) examined cases from multiple studies and found that the mean velocity profile in defect coordinates was essentially the same for all equilibrium turbulent FPG boundary layers, regardless of the strength of the FPG. The Spalart (1986) DNS results indicate that some differences in the defect profiles are apparent as K is varied, particularly in the inner region, but that the differences are vanishingly small for $y/\delta > 0.2$, where y is the wall-normal distance and δ is the 99 % boundary-layer thickness. In inner coordinates the variation with K is clearer, with the mean profile rising above the ZPG law of the wall in the log region, as shown in studies such as Jones & Launder (1972), Spalart (1986) and Dixit & Ramesh (2008). The non-equilibrium region between the beginning of a sink flow FPG and the attainment of equilibrium depends on the upstream condition and the strength of the pressure gradient. In mild to moderate pressure gradients, studies such as Jones, Marusic & Perry (2001) and Volino (2020) showed a monotonic progression from ZPG conditions towards an equilibrium sink flow. The mean velocity deficit gradually decreased while β increased in magnitude or remained nearly constant at the equilibrium value. In stronger FPG cases, Volino (2020) saw β dropping from higher magnitudes toward the equilibrium $\beta = -0.6$, and the mean velocity deficit decreasing from the ZPG value past the sink flow equilibrium and then increasing back towards the equilibrium value.

Many flows of interest occur on rough surfaces, and several studies have considered the combined effects of roughness and FPGs. Coleman, Moffat & Kays (1977) proposed conditions for equilibrium on rough walls, which required a variable K. Tachie & Shah (2008) considered mild FPG cases and saw that in the near-wall region differences between the ZPG and FPG cases were small, with the roughness effect dominating over the pressure gradient effect. In the outer part of the flow, the FPG reduced the Reynolds stresses. Cal *et al.* (2009) considered cases with K below 0.5×10^{-6}. As with a smooth wall, the pressure gradient decreased the mean velocity deficit and the Reynolds stresses. Volino & Schultz (2023) investigated rough-wall cases with constant K ranging from 0.125×10^{-6} to 2×10^{-6}. When normalised using δ and u_τ, the mean velocity and Reynolds stress results agreed with those from comparable smooth-wall cases, indicating that the outer-layer similarity between rough- and smooth-wall cases described by Townsend (1976) for ZPG flows continues to apply for FPG conditions.

Only a few studies have considered rough-wall boundary layers with $K > 3 \times 10^{-6}$ (i.e. large enough to cause relaminarisation in a smooth-wall case). Yuan & Piomelli (2015) reported DNS results for spatially developing boundary layers. The pressure gradient matched the smooth-wall experiment of Warnack & Fernholz (1998), with K increasing from 0 to 4×10^{-6} and then decreasing back to zero. In the smooth-wall

case, relaminarisation was observed. For the rough wall, the roughness Reynolds number, $k^+ = ku_\tau/\nu$, with k the average roughness height, rose from 23 to 80, going from the transitionally rough regime to fully rough. For the surface simulated, the equivalent sandgrain roughness, k_s, was equal to $1.6k$. The acceleration increased the shear rate at the wall and caused the roughness effect to increase. The skin friction coefficient increased continuously as K increased, while k/δ increased as the boundary layer became thinner. The boundary layer did not relaminarise. The Reynolds stresses decreased relative to the increasing ${u_\tau}^2$, but still remained significant. The roughness resulted in turbulence production in the near-wall region, in spite of the strong FPG. Relaminarisation was only expected to occur if the roughness was small enough for the wall to be considered hydraulically smooth.

The rough-wall equilibrium sink flow case was considered by Yuan & Piomelli (2014). In equilibrium, all dimensionless quantities, including k/δ, are constant. The DNS and large-eddy simulations, therefore, were equivalent to a spatially evolving boundary layer with k decreasing linearly in the streamwise direction to match the decreasing boundary-layer thickness. They considered K values from 0.45×10^{-6} to 2.50×10^{-6}. The roughness modelled was sandgrain with k/δ between 0.015 and 0.04 and k^+ between 10 and 42, indicating transitionally rough conditions. Full reverse transition did not occur in any case, but a case with the strongest K and $k^+ = 13$ was close to hydraulically smooth conditions and showed some signs of relaminarisation.

While the equilibrium sink flow case is interesting, a more physically likely surface would have uniform roughness. When subject to a constant K acceleration, the ratio k/δ would continuously increase as δ decreased in the streamwise direction. Such a surface might approach a quasi-equilibrium as long as k/δ remained sufficiently small. If hydraulically smooth, relaminarisation could potentially occur. Eventually, however, as k/δ became continuously larger, any quasi-equilibrium would presumably be broken. The present study considers a spatially developing sink flow with uniform random roughness. The acceleration parameter is set to $K = 3.2 \times 10^{-6}$, which is large enough to cause relaminarisation on a smooth wall. It appears that such a case has not been reported in the literature. Two sizes of roughness are used, one intended to produce transitionally rough conditions and the other fully rough. A smooth-wall case is also included for comparison. The spatial development of the boundary layers is documented to show the progression from an initial ZPG condition.

2. Experiments

Experiments were conducted in the recirculating water tunnel described in Volino (2020). Water was supplied to the test section from a 4000 l cylindrical tank via two variable-speed pumps operating in parallel and a flow conditioning section consisting of a honeycomb and three screens followed by a three-dimensional contraction and a second honeycomb. Following the test section the water returned through a perforated plate into the cylindrical tank. The free-stream turbulence intensity was 0.3 % in the test section. The test fluid was filtered and deaerated water. A chiller was used to keep the water temperature constant to within 0.5 °C. The test section was 0.2 m wide, 2 m long and 0.1 m tall at the inlet. The bottom surface of the test section was the flat test wall and included a trip at the leading edge, as shown in figure 1. The upper surface consisted of four flat plates that could be independently adjusted to set the pressure gradient. The sidewalls and upper wall were transparent for optical access.

The inlet velocity to the test section was set to 0.5 m s^{-1} in all cases. A ZPG was set for the first 0.6 m downstream of the trip to establish a canonical ZPG boundary layer.

Surface	k_a (mm)	k_{rms} (mm)	k_t (mm)	Sk	Fl	ES	k_s (mm)
$Sk = -1$	0.276	0.350	3.45	−0.97	4.17	0.40	0.60
$Sk = +1$	0.277	0.350	3.47	+ 0.98	4.18	0.40	2.0

Table 1. Roughness surface statistics. Parameters: k_a, mean amplitude; k_{rms}, root-mean-square height; k_t, average peak-to-trough height; Sk, skewness; Fl, flatness; ES, effective slope; k_s, equivalent sandgrain roughness height.

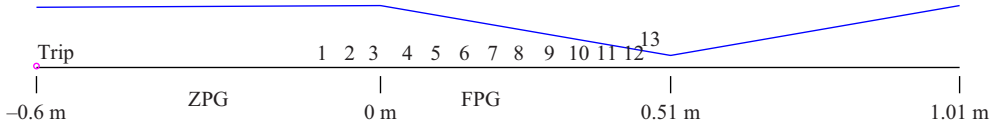

Figure 1. Cross-section of the test section in the streamwise–wall-normal plane. Numbers in the test section indicate streamwise measurement stations. Shown approximately to scale.

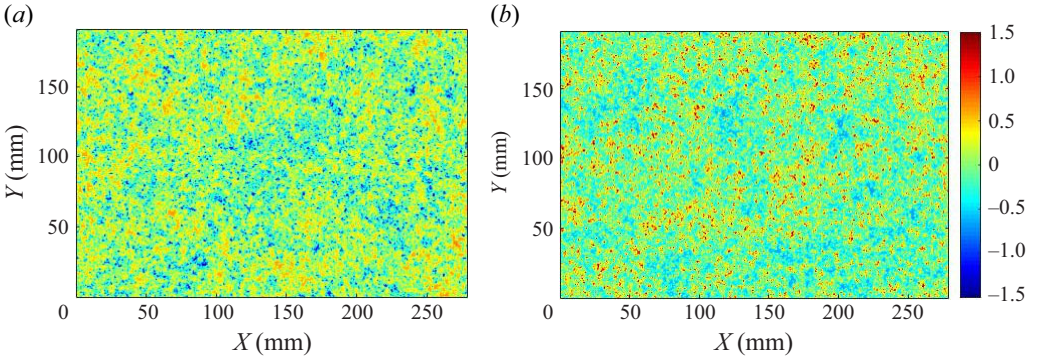

Figure 2. Elevation maps for sections of rough surfaces: (*a*) $Sk = -1$; (*b*) $Sk = +1$. Height indicated by colour bar in mm.

This was followed by a 0.5 m long FPG section set for $K = 3.2 \times 10^{-6}$. The FPG was followed by an adverse-pressure-gradient section, as shown in figure 1, that was used as a diffuser before the flow was returned to the cylindrical tank.

The test wall consisted of a 0.23 m long smooth section followed by a replaceable downstream section where roughness could be included. An acrylic plate was used for the smooth-wall case. For the two rough-wall cases, additively manufactured plates with the mathematically generated three-dimensional random roughness described in Flack, Schultz & Volino (2020) were used. The statistics for these surfaces are given in table 1, and the geometry is shown in figure 2. The two roughnesses differed in their skewness, Sk, with one having $Sk = +1$ and the other $Sk = -1$. The average equivalent sandgrain roughness was estimated based on the ZPG velocity profiles of Flack *et al.* (2020), Volino & Schultz (2022) and the present study using the relation between the roughness function, ΔU^+, and k_s:

$$\Delta U^+ = \frac{1}{\kappa} \ln\left(k_s^+\right) + B - 8.5. \tag{2.1}$$

The roughness function is the downward displacement of the log region of the mean velocity profile in inner coordinates below the smooth-wall law of the wall. The values

used for κ and B are 0.384 and 4.17, respectively. The average k_s values used below are 2 mm for the $Sk = +1$ surface and 0.6 mm for the $Sk = -1$ surface.

Velocity profiles were acquired at 13 streamwise stations along the spanwise centreline of the test section using a TSI FSA3500 two-component laser Doppler velocimeter. A four-beam fibre optic probe was used to collect data in backscatter mode. The beams entered the test section through one sidewall. A custom-designed beam displacer was used to shift one of the four beams, resulting in three co-planar beams that were aligned parallel to the test wall. A 2.6 : 1 beam displacer was located at the exit of the probe to reduce the size of the measurement volume to 45 μm in diameter and 340 μm long. The flow was seeded with 2 μm diameter silver-coated glass spheres. Data were acquired at 43 locations within each velocity profile using a traverse with 6.25 μm resolution to move the probe from the wall to the free stream. At each location, data were acquired for 10 000 large-eddy turnover times, δ/U_e. The uncertainty in the mean streamwise velocity was 0.5 % of U_e. The 95 % confidence interval uncertainty in the Reynolds stresses ranged from 1 % to 4 %. More details of the uncertainty analysis are available in Volino & Schultz (2022).

Because of the pressure gradient and test section geometry, the free-stream velocity varied slightly in the wall-normal direction. The variation was very nearly linear. To determine the 99 % boundary-layer thickness, a straight line was fitted through the measured velocity points in the free stream for each profile, and a line at 99 % of the fit line was extrapolated to the wall. The location where the measured velocity intersected the 99 % line was taken as the boundary-layer thickness, δ.

The friction velocity was found from each velocity profile using the method described by Volino & Schultz (2018) with an uncertainty of 5 %. The method is based on the streamwise momentum equation and uses the measured mean streamwise velocity and Reynolds shear stress profiles. The effective location of $y = 0$ for each profile was found by shifting the data in the wall-normal direction until the near-wall data agreed with a log law as closely as possible. The data were not forced to agree with the standard ZPG log-law slope, since the slope could be different in an FPG. The average shift was 0.09 mm for the smooth-wall case, 0.18 mm for the $Sk = -1$ rough-wall case and 0.85 mm for the $Sk = +1$ case.

3. Results

3.1. *Comparison cases*

To assess the state of the boundary layer with respect to equilibrium and relaminarisation, it is useful to have equilibrium sink flow comparison cases. As noted above, an exact solution exists for the mean velocity profile in the laminar case, and various quantities such as the skin friction coefficient can be found as functions of K. For turbulent cases, DNS solutions are available up to $K = 2.75 \times 10^{-6}$, but above this, turbulence cannot be sustained on a smooth wall. On a rough wall, however, the boundary layer can remain turbulent, so it is useful to know how dependent the solution is on K, and whether the DNS result at $K = 2.75 \times 10^{-6}$ might be useful for comparison with experiments at higher K. The results of Spalart (1986) and Castillo & George (2001), mentioned above, indicate that the mean profile for an FPG boundary layer is largely independent of K. This is illustrated and checked for other quantities in figure 3, which compares the equilibrium DNS results of Spalart (1986) at $K = 1.5 \times 10^{-6}$, 2.5×10^{-6} and 2.75×10^{-6} with experimental data from the literature at various K values. Mean velocity profiles in defect coordinates are shown in figure 3(*a*). There is little difference between the DNS profiles. The experiments of Jones *et al.* (2001) agree closely with the DNS, in spite of an

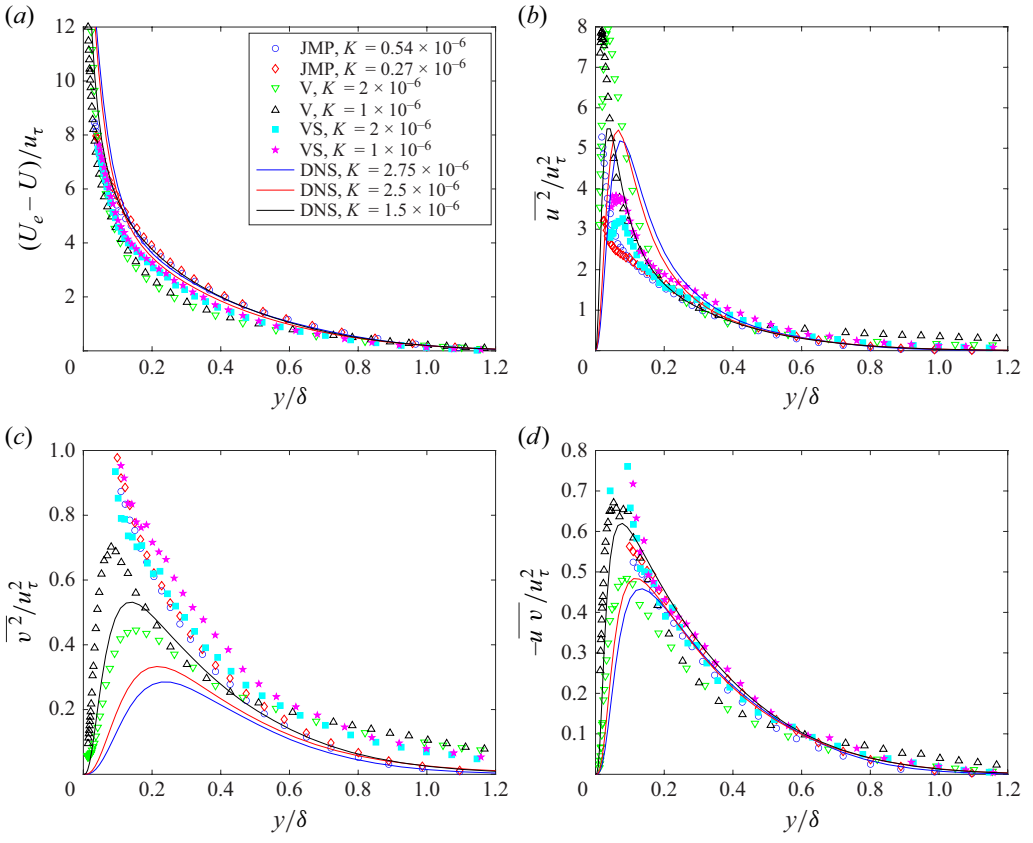

Figure 3. Comparison of experimental turbulent sink flow data of Jones *et al.* (2001) (JMP, smooth wall), Volino (2020) (V, smooth wall) and Volino & Schultz (2023) (VS, rough wall) with equilibrium sink flow DNS of Spalart (1986). (*a*) Mean streamwise velocity, (*b*) streamwise Reynolds normal stress, (*c*) wall-normal Reynolds normal stress and (*d*) Reynolds shear stress.

order-of-magnitude difference in K. The smooth-wall results of Volino (2020) fall below those of the DNS. As discussed in Volino (2020), the Jones *et al.* (2001) cases approached equilibrium monotonically, with Re_θ increasing to the equilibrium value and the velocity defect dropping from the upstream ZPG condition to equilibrium at the location of the profiles shown. In the Volino (2020) cases, Re_θ was dropping and the boundary layer had not yet reached equilibrium. Computations suggested that this boundary layer had overshot the equilibrium profile and would have risen back to match it if given further streamwise distance to develop. The rough-wall cases of Volino & Schultz (2023) behaved similarly.

The streamwise component of the Reynolds normal stress, $\overline{u'^2}^+$, is shown in figure 3(*b*). All of the experimental cases collapse for $y/\delta > 0.15$ and agree best with the lowest-K DNS result. Close to the wall there is more variation between the experimental cases and K dependence for the DNS. The wall-normal component of the Reynolds stress, $\overline{v'^2}^+$, is shown in figure 3(*c*). There is clear K dependence for the DNS. The Reynolds shear stress, $-\overline{u'v'}$, in figure 3(*d*) shows less K dependence for $y/\delta > 0.2$ in both the experimental and DNS results. The smooth-wall cases from Volino (2020) lie below the others, showing the same overshoot of equilibrium noted in the mean velocity profiles, but the other cases are in good agreement with each other and the DNS.

The results indicate that at least for the mean profile and the Reynolds shear stress, the equilibrium turbulent sink flow profiles do not depend strongly on K. The $K = 2.75 \times 10^{-6}$ DNS results are shown for reference in the figures below.

3.2. *Present results with $K = 3.2 \times 10^{-6}$*

Boundary-layer parameters for the three experimental cases are given in table 2. The momentum thickness Reynolds number and friction Reynolds numbers are shown in figure 4. In the smooth-wall case, Re_θ drops from a ZPG value of 1100 to 600 at $x/x_{sink} = 0.4$. The origin for x is taken as the start of the FPG. The expected equilibrium value for a turbulent boundary layer at $K = 3.2 \times 10^{-6}$ is about $Re_\theta = 310$. Downstream there is a more sudden drop to $Re_\theta = 264$ at the last station. The laminar equilibrium sink flow solution is $Re_\theta = 0.3754K^{-0.5} = 210$. The behaviour is similar in Re_τ, dropping after $x/x_{sink} = 0.4$ towards a value of about 184. The laminar equilibrium sink flow value is $Re_\tau = 3.635K^{-0.25} = 86$. This suggests the smooth-wall case is approaching but has not yet reached the laminar equilibrium state. In the rough-wall cases, Re_θ drops from the ZPG value to about 600 in the $Sk = -1$ case and to about 900 in the $Sk = +1$ case. Both show a slight increase at the most downstream stations. The Re_τ values for both cases remain fairly constant, with an increase in the $Sk = +1$ case at the downstream stations. The shape factor, $H = \delta^*/\theta$, provides another view of the state of the boundary layer, and is shown in figure 5. The H values are about the same for the smooth-wall and $Sk = -1$ cases from the ZPG region to $x/x_{sink} = 0.4$. This suggests that roughness is small enough that it is not having a large effect on the boundary layer, which is consistent with the Reynolds numbers of figure 4, which are not very much higher for the $Sk = -1$ case compared with the smooth-wall case. The streamwise drop in H is consistent with expectations for a turbulent FPG boundary layer. The $Sk = +1$ roughness causes higher H but the behaviour is otherwise similar, with a drop from the upstream ZPG value. Downstream of $x/x_{sink} = 0.4$, H rises in all cases. In the smooth-wall case it rises to $H = 1.71$, which compares with the laminar equilibrium sink flow value of $H = 2.07$. It appears that H rises in the rough-wall cases because the roughness effect is increasing as the boundary layer becomes thinner, while in the smooth-wall case it increases because the boundary layer is approaching a laminar-like state.

The results in figures 4 and 5 suggest that the boundary layer is relaminarising in the smooth-wall case and is approaching the expected equilibrium. The onset of relaminarisation appears to be somewhat abrupt, occurring near $x/x_{sink} = 0.4$. In the rough-wall cases, the boundary layer appears to remain turbulent. This is supported by the skin friction coefficient, shown in figure 6. In the smooth-wall case, the upstream value of C_f is 0.0043, which is consistent with expectations for a turbulent ZPG boundary layer at the corresponding Re_θ. The value remains essentially constant, and at the downstream stations matches the expected laminar sink flow value of $C_f = 2.30K^{0.5} = 0.0041$. It is coincidental that the upstream and downstream values are equal. In the rough-wall cases, C_f rises in the streamwise direction. It appears to be levelling off towards an equilibrium in the $Sk = -1$ case, but is still rising in the $Sk = +1$ case. Figure 7, which compares the roughness height with the boundary-layer thickness, may provide some explanation. In the $Sk = -1$ case, k_s^+ rises from a transitionally rough value of 16 to a fully rough value of 100. The low upstream value is consistent with the similarity observed in figure 6 between this case and the smooth-wall case, while the downstream value is consistent with the boundary layer remaining turbulent while the smooth-wall case relaminarised. The ratio of δ/k_s continuously drops, but is still above five at the last measurement station. Although

Station	x (m)	U_e (m s^{-1})	u_τ (m s^{-1})	δ (mm)	Re_θ	Re_τ	H
Smooth							
1	−0.10	0.500	0.0232	17.52	1110	417	1.45
2	−0.05	0.502	0.0233	17.98	1138	434	1.45
3	−0.01	0.512	0.0240	18.00	1117	446	1.43
4	0.05	0.542	0.0260	17.40	1053	468	1.38
5	0.10	0.585	0.0270	16.33	955	457	1.36
6	0.15	0.636	0.0300	13.84	779	428	1.36
7	0.20	0.705	0.0340	12.19	667	430	1.37
8	0.25	0.798	0.0360	10.99	616	410	1.40
9	0.30	0.908	0.0430	7.47	436	333	1.46
10	0.35	1.082	0.0520	6.03	371	326	1.53
11	0.40	1.340	0.0615	5.01	356	319	1.54
12	0.45	1.738	0.0780	3.04	311	246	1.63
13	0.475	2.025	0.0915	1.93	264	184	1.71
Rough $Sk = -1$							
1	−0.10	0.503	0.0260	18.44	1237	493	1.46
2	−0.05	0.507	0.0260	18.64	1258	501	1.46
3	−0.01	0.516	0.0260	18.59	1255	501	1.43
4	0.05	0.548	0.0320	18.03	1188	597	1.39
5	0.10	0.592	0.0330	16.84	1069	575	1.34
6	0.15	0.648	0.0390	14.91	945	602	1.37
7	0.20	0.722	0.0470	13.76	885	671	1.34
8	0.25	0.807	0.0510	11.05	740	584	1.40
9	0.30	0.931	0.0670	9.87	715	684	1.37
10	0.35	1.082	0.0840	5.57	595	484	1.48
11	0.40	1.348	0.1120	4.66	601	540	1.47
12	0.45	1.765	0.1430	3.30	581	489	1.46
13	0.475	2.046	0.1600	3.49	726	578	1.48
Rough $Sk = +1$							
1	−0.10	0.503	0.0320	19.75	1442	648	1.66
2	−0.05	0.502	0.0320	20.17	1526	670	1.65
3	−0.01	0.510	0.0315	20.19	1497	660	1.58
4	0.05	0.536	0.0440	19.45	1458	886	1.60
5	0.10	0.577	0.0460	18.39	1352	876	1.51
6	0.15	0.635	0.0520	16.40	1177	881	1.49
7	0.20	0.703	0.0520	14.12	1051	762	1.42
8	0.25	0.799	0.0620	12.18	957	784	1.44
9	0.30	0.911	0.0900	10.02	972	927	1.63
10	0.35	1.084	0.1100	6.82	849	775	1.69
11	0.40	1.344	0.1310	5.83	922	791	1.63
12	0.45	1.770	0.2100	5.47	1163	1190	1.79
13	0.475	2.064	0.2250	4.20	1055	977	1.72

Table 2. Boundary-layer parameters.

the ratio is well below the recommended value of about 40 needed to ensure outer and inner scale separation (Jiménez 2004), it may still be high enough that the boundary layer is able to reach a quasi-equilibrium sink flow condition. In the $Sk = +1$ case, $k_s{}^+ > 65$, so fully rough behaviour is anticipated. The δ/k_s ratio drops as low as two, which appears to be too low for establishment of a quasi-equilibrium. Hence the continuously rising C_f in this case.

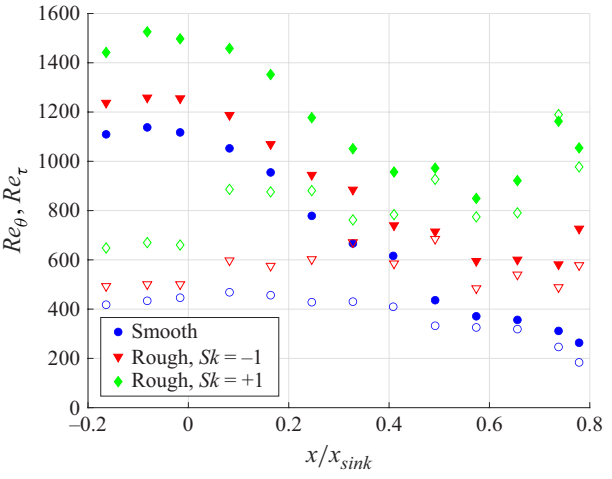

Figure 4. Momentum thickness Reynolds number (filled symbols) and friction Reynolds number (open symbols) for the present study.

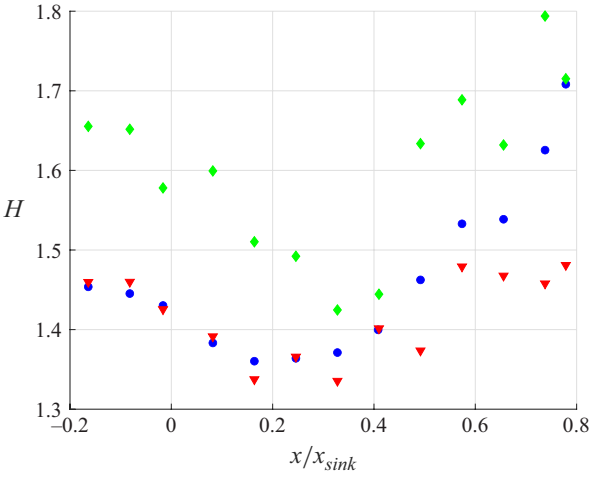

Figure 5. Shape factor. Legend as in figure 4.

3.3. *Mean velocity*

To show how the state of the boundary-layer changes, mean velocity profiles are considered next. Figure 8(*a*) shows the profiles for the smooth-wall case in inner coordinates. The streamwise stations correspond to the streamwise locations shown in figure 1 and to the points in figures 4–7. The profiles agree well with the turbulent law of the wall at the upstream ZPG stations. At stations 4–6, the profiles rise above the standard log law and appear to reach a new equilibrium, as expected for a turbulent sink flow (e.g. Jones & Launder 1972). The sink flow profile for $K = 2.75 \times 10^{-6}$ from Spalart (1986) is shown for comparison. In these coordinates the equilibrium profile depends on K, so it is reasonable that the experimental profiles should lie above the $K = 2.75 \times 10^{-6}$ result. Between stations 7 and 8, a change occurs. This location corresponds to the drop in Reynolds number at $x/x_{sink} = 0.4$ seen in figure 4. The profiles continue to rise and appear to reach

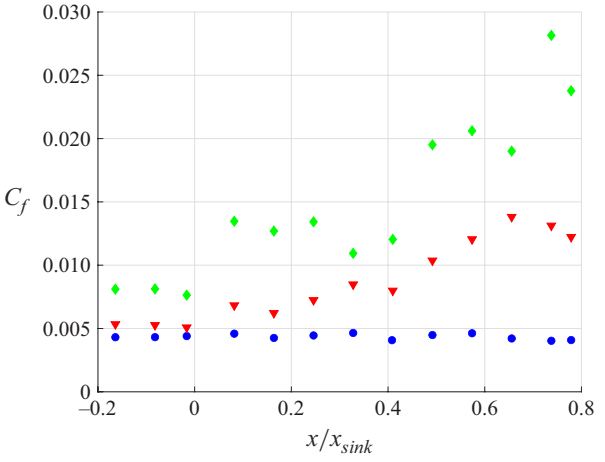

Figure 6. Skin friction coefficient. Legend as in figure 4.

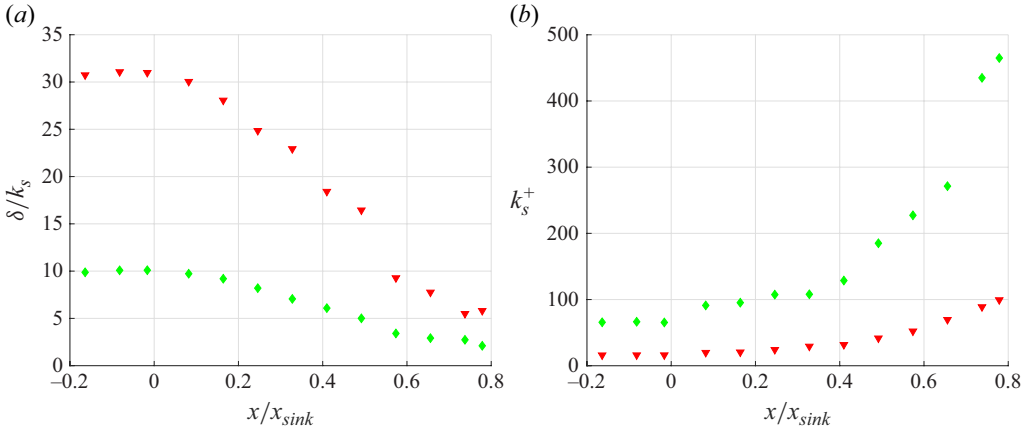

Figure 7. Roughness height: (*a*) δ/k_s; (*b*) $k_s{}^+$. Legend as in figure 4.

a new equilibrium at stations 12 and 13 that agrees with the laminar equilibrium sink flow solution.

The profiles are shown in defect coordinates in figures 8(*b*) and 8(*c*). The velocity defect decreases, as expected for an FPG, and appears to reach a temporary equilibrium at stations 7 to 11. These profiles lie below the DNS solution. The overshoot of the turbulent equilibrium result agrees with the cases of Volino & Schultz (2023) in figure 3. Downstream of station 11 the profiles begin to rise but do not reach the laminar sink flow solution, consistent with the results of figures 4 and 5. Cal & Castillo (2008) describe similar behaviour for smooth-wall cases.

Results for the $Sk = -1$ case are shown in figure 9. In inner coordinates the profiles are shifted upward by the roughness function given by (2.1). Since (2.1) is based on fully rough ZPG results, there is no reason to presume it must apply in the present transitionally rough FPG boundary layer, but it does collapse the results to within the experimental uncertainty. The FPG suppresses the wake seen at the ZPG stations. The profiles at most stations lie above the standard log law, in agreement with the DNS sink flow result. At stations 4–8 the near-wall data show signs of a viscous sublayer, which is possible since $k_s{}^+ < 32$ at

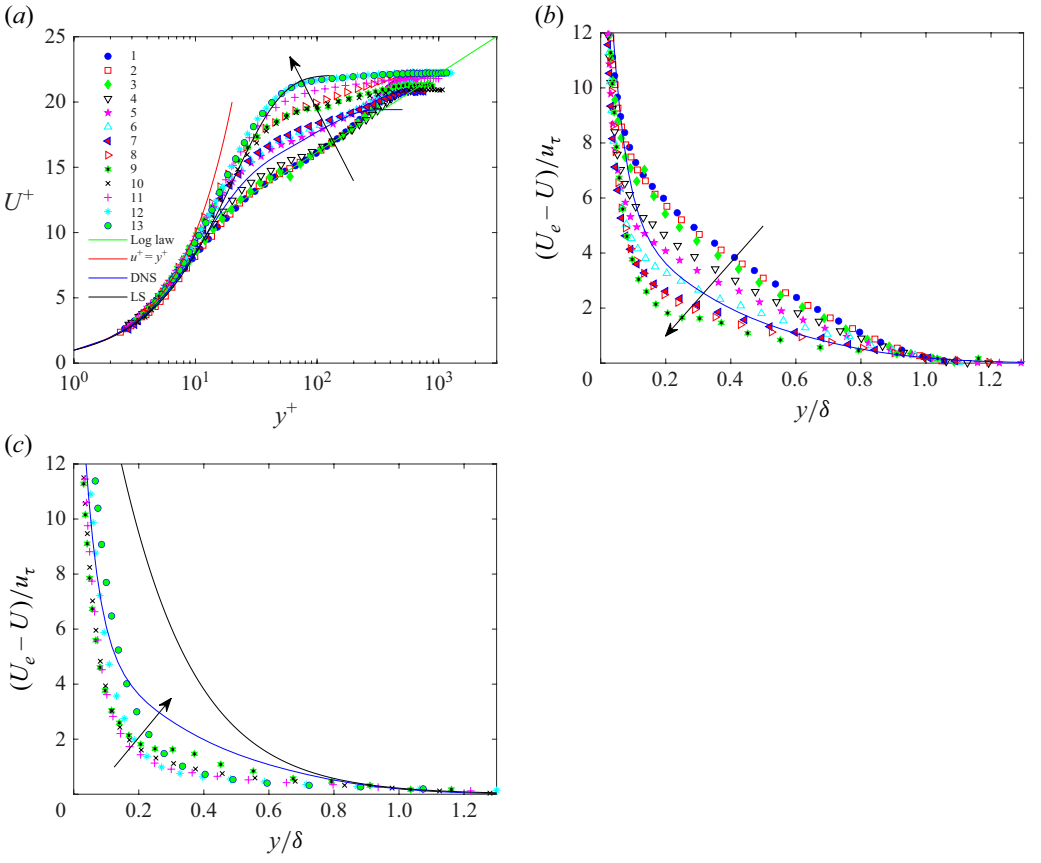

Figure 8. Mean streamwise velocity profiles for smooth-wall case: (*a*) inner coordinates; (*b*) defect coordinates for stations 1–9; (*c*) defect coordinates for stations 9–13. Legend indicates streamwise station. DNS is $K = 2.75 \times 10^{-6}$ equilibrium sink flow simulation from Spalart (1986). Here LS is laminar equilibrium sink flow solution. Arrows indicate progression of profiles in the streamwise direction.

these stations. The outer region shows no sign of relaminarising at any location. In defect coordinates the profiles shift downward through station 9, agreeing with the smooth-wall results of figure 8. At stations 10–13 there is a very slight upward shift of the profiles. Since this shift is within the uncertainty, it may not be significant, but it could indicate a reversal of the overshoot and return towards the turbulent sink flow result. Another possibility is that the rise is caused by an increased roughness effect as δ/k_s decreases. The mean profiles for the $Sk = +1$ case are shown in figure 10. The results are essentially the same as those of figure 9, with the exception that in inner coordinates the scatter between stations is larger, presumably because ΔU^+ is significantly larger.

3.4. *Reynolds stresses*

Profiles of $\overline{u'^2}^+$ are shown for the smooth-wall case in figure 11. For stations 1–8, the inner peak is unchanged while the turbulence is suppressed in the outer region. These are expected results for a turbulent FPG boundary layer, and are consistent with the mean velocity profiles. For $y/\delta < 0.2$ the data show the same drop below the DNS solution as in the fully turbulent cases of figure 3(*b*). Farther from the wall the data are above the

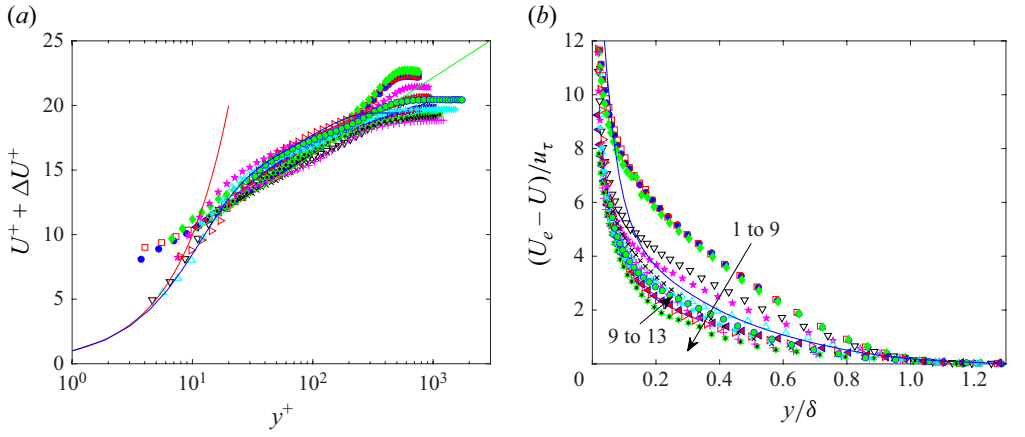

Figure 9. Mean streamwise velocity profiles for $Sk = -1$ case: (*a*) inner coordinates; (*b*) defect coordinates. Legend as in figure 8. Arrows indicate progression of profiles in the streamwise direction through station numbers indicated.

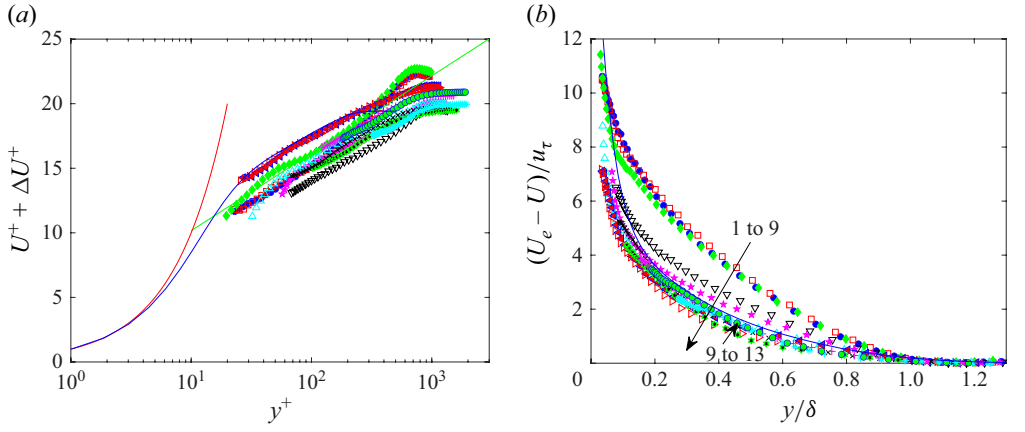

Figure 10. Mean streamwise velocity profiles for $Sk = +1$ case: (*a*) inner coordinates; (*b*) defect coordinates. Legend as in figure 8. Arrows indicate progression of profiles in the streamwise direction through station numbers indicated.

DNS result. This is believed to be an artefact of the measurement technique. The actual free-stream turbulence level in this facility, as measured with a particle image velocimetry system, was about 0.3 %. As explained by DeGraaff (1999), laser Doppler velocimetry systems with small probe volumes produce artificially high turbulence readings that scale with the local mean velocity. The resulting error is insignificant in comparison with the actual turbulence in most of the boundary layer, but is significant near the edge of the boundary layer, where the actual turbulence is low. The noise is uncorrelated in the two velocity components, so it does not affect the Reynolds shear stress.

Downstream of station 8, the behaviour changes, as shown in figure 11(*b*). The peak drops, while the profiles rise somewhat in the outer region. This is the region where the mean profiles of figure 8 indicate relaminarisation. The change in the $\overline{u'^2}^+$ profiles at the downstream stations is due mainly to the increase in u_τ. In dimensional coordinates the profiles at the downstream stations do not change much. This is the quasi-laminar state

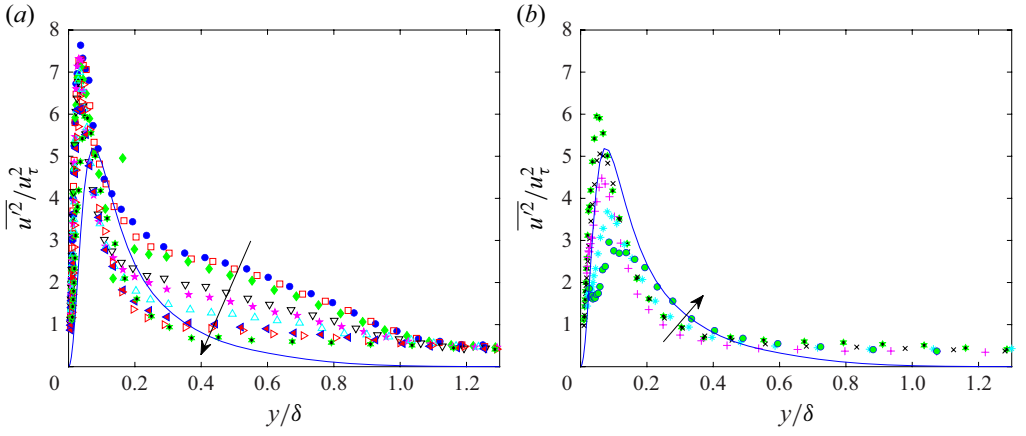

Figure 11. Streamwise Reynolds normal stress profiles for smooth-wall case: (*a*) stations 1–9; (*b*) stations 9–13. Legend as in figure 8. Arrows indicate progression of profiles in the streamwise direction.

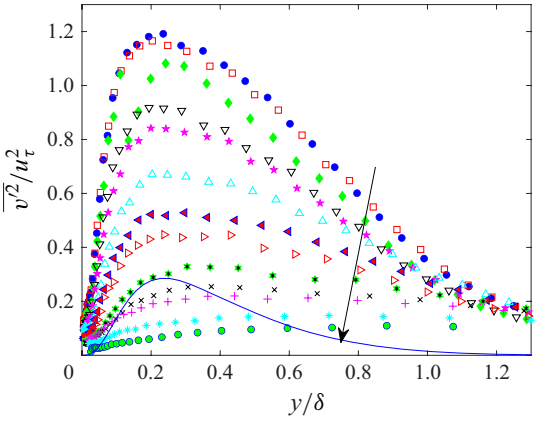

Figure 12. Wall-normal Reynolds normal stress profiles for smooth-wall case. Legend as in figure 8. Arrow indicates progression of profiles in the streamwise direction.

described by Piomelli & Yuan (2013) and others. The turbulence is essentially frozen, and the fluctuations acting across an increasingly large wall-normal mean streamwise velocity gradient result in significant u' fluctuations. Bradshaw (1967) referred to turbulent motions that do not produce shear stress as inactive, and this applies to much of the present u' fluctuations, as indicated by the other components of the Reynolds stress. Since the motions are inactive, the mean profile can still relaminarise.

Figure 12 shows the wall-normal component of the Reynolds normal stress. The profile peaks decrease steadily in the streamwise direction. Figure 13 shows profiles of the ratio of $\overline{u'^2}^+$ to $\overline{v'^2}^+$, illustrating the changing anisotropy of the turbulence. From stations 1 to 7 the ratio remains between 2 and 2.5 for $y/\delta > 0.2$ and rises to a peak at $y/\delta \approx 0.02$, with the magnitude of the peak increasing from about 30 in the upstream ZPG to about 70 at station 7. Beginning at station 6 the near-wall peak begins to widen, and the widening becomes more rapid beyond station 8 and extends into the outer part of the boundary layer. This corresponds to the beginning of the relaminarisation, in which the inactive u' fluctuations continue to scale with the increasing velocity gradient, while the v' fluctuations remain

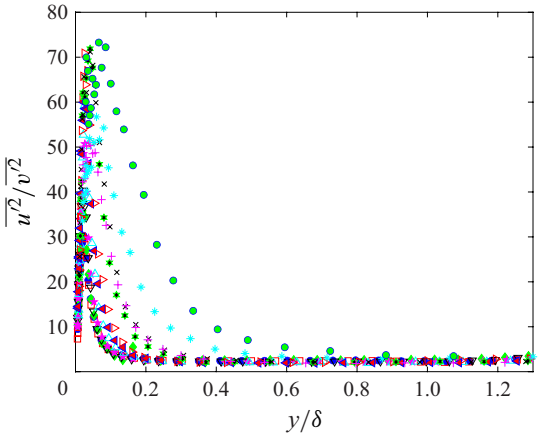

Figure 13. Profiles of $\overline{u'^2}/\overline{v'^2}$ ratio for smooth-wall case. Legend as in figure 8.

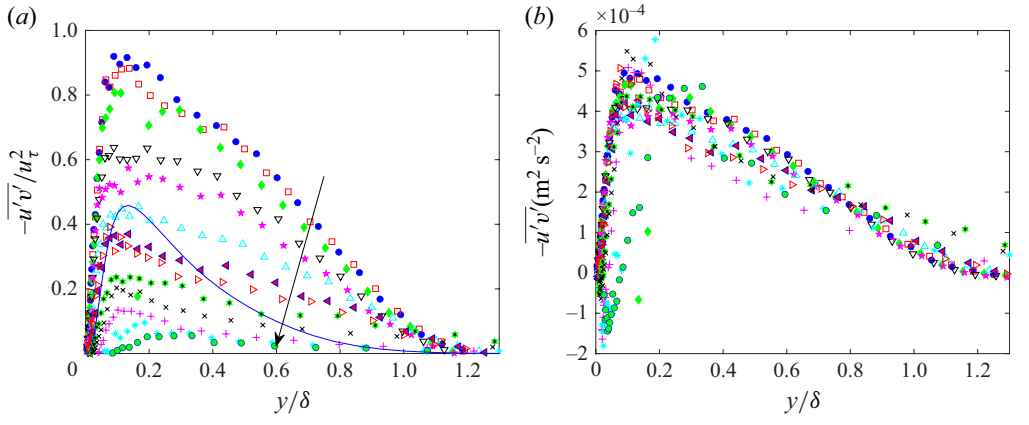

Figure 14. Reynolds shear stress profiles for smooth-wall case: (*a*) dimensionless; (*b*) dimensional. Legend as in figure 8. Arrow indicates progression of profiles in the streamwise direction.

frozen at the upstream magnitude. Since the active motions are of most importance for turbulent mixing and the development of the boundary layer, they are the focus of much of the discussion below.

The Reynolds shear stress, shown in figure 14, exhibits the same behaviour as $\overline{v'^2}^+$. Of note is the agreement of the profiles at stations 7 and 8, followed by the significant drop, particularly in the near-wall region, and the outward shift of the peaks farther downstream. The agreement at stations 7 and 8 may indicate an approach to a turbulent quasi-equilibrium, and the downstream drop corresponds to the beginning of relaminarisation. Figure 14(*b*) shows $-\overline{u'v'}$ dimensionally. The profiles at the first 10 stations collapse. The FPG prevents $-\overline{u'v'}$ from growing with the increasing wall shear, but it does not go away. It is large enough to maintain a turbulent boundary layer for some distance, but it becomes increasingly insignificant as the mean velocity increases. Eventually the level, particularly near the wall, becomes too small, and the boundary layer relaminarises. There is never agreement with the equilibrium turbulent DNS solution. At the upstream stations

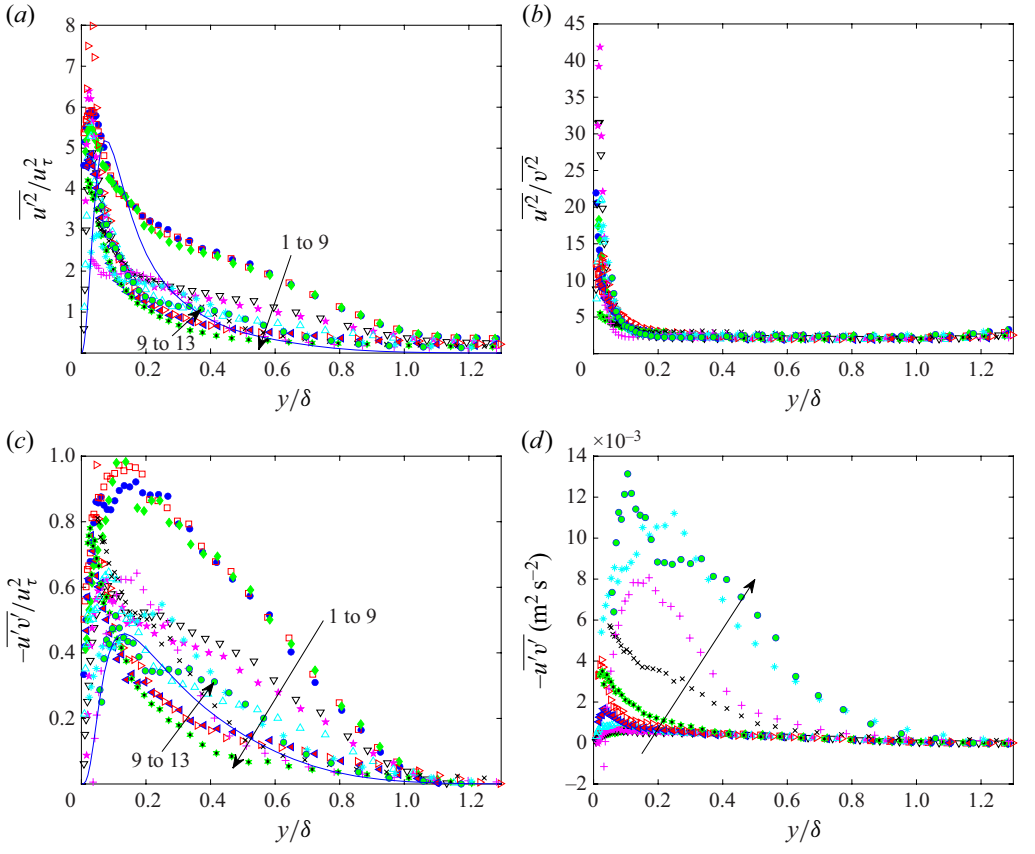

Figure 15. Reynolds stress profiles for $Sk = -1$ case: (*a*) $\overline{u'^2}^+$; (*b*) $\overline{u'^2}/\overline{v'^2}$ ratio; (*c*) $-\overline{u'v'}^+$; (*d*) dimensional $-\overline{u'v'}$. Legend as in figure 8. Arrows indicate progression of profiles in the streamwise direction through station numbers indicated.

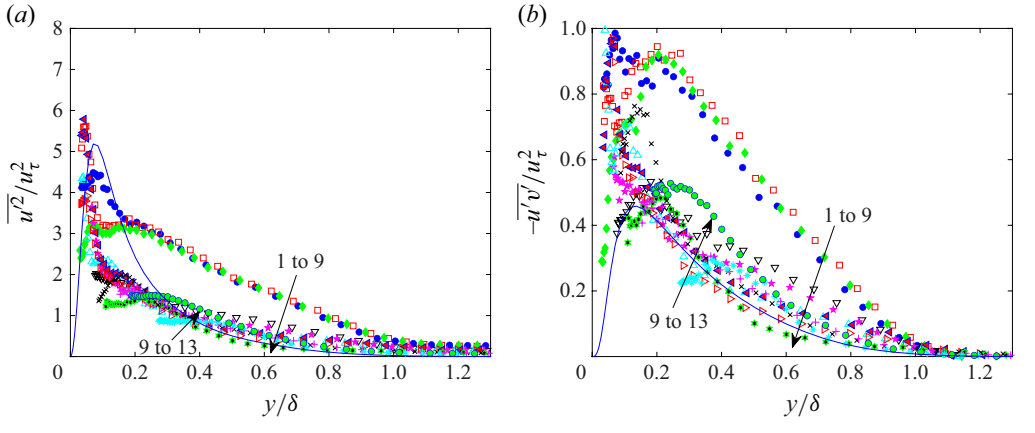

Figure 16. Reynolds stress profiles for $Sk = +1$ case: (*a*) $\overline{u'^2}^+$; (*b*) $-\overline{u'v'}^+$. Legend as in figure 8. Arrows indicate progression of profiles in the streamwise direction through station numbers indicated.

the boundary layer is still turbulent, but has not reached equilibrium, so the data lie above the DNS curve. Downstream, after relaminarisation begins, the data lie below the turbulent solution.

The $Sk = -1$ rough-wall Reynolds stress profiles are shown in figure 15. The $\overline{u'^2}^+$ results are similar to those of the smooth-wall case in figure 11(*a*) and the fully turbulent cases of figure 3(*b*). The near-wall peak would be suppressed for fully rough conditions, but since the present case is transitionally rough, the peak is clear at some stations. This is in agreement with the appearance of a sublayer in the mean profiles of figure 8. At the downstream stations, the rough- and smooth-wall cases are different. In the near-wall region, $\overline{u'^2}^+$ is higher for the rough-wall case, consistent with the boundary layer remaining turbulent. There is a slight rise in $\overline{u'^2}^+$ between stations 9 and 13 in figure 15(*a*). This may be due to a closer approach to a turbulent quasi-equilibrium, or it may be due to an increased roughness effect as δ and δ/k_s decrease.

The ratio of $\overline{u'^2}$ to $\overline{v'^2}$ is shown in figure 15(*b*). Similar to the upstream stations of the smooth-wall case, the ratio is about 2.5 for $y/\delta > 0.2$ and rises to a peak near the wall. Unlike the smooth-wall case, the ratio does not rise at the downstream stations, because the boundary layer remains turbulent in the rough-wall case. The u' and v' fluctuations remain correlated and related to active motions.

The Reynolds shear stress for the $Sk = -1$ case is shown in figure 15(*c*). The $\overline{v'^2}^+$ normal stress profiles are very similar to the $-\overline{u'v'}^+$ profiles and are not presented. The behaviour is essentially the same as in $\overline{u'^2}^+$, again showing that u' remains related to active motions in this case. The profiles drop below the equilibrium DNS at stations 7–9, and then rise slightly above it at stations 10–13. The dimensional $-\overline{u'v'}$ is shown in figure 15(*d*), and it rises rapidly in response to the rising wall shear. Reynolds shear stress is clearly being produced in the turbulent boundary layer, unlike the frozen turbulence of the smooth-wall case of figure 14(*b*).

Results for the $Sk = +1$ case are shown in figure 16. Comparing with figure 15, the inner peak is more suppressed because of the larger roughness, and in the outer region there is less of a drop below the sink flow DNS at stations 7–9, perhaps because the larger roughness is mitigating some of the effect of the FPG and limiting the overshoot of the smooth-wall equilibrium. At the most downstream station, the larger roughness causes a higher $-\overline{u'v'}^+$ peak in the $Sk = +1$ case. This may indicate a departure from quasi-equilibrium as δ/k_s approaches two. The $\overline{u'^2}$ to $\overline{v'^2}$ ratio is essentially the same as for the $Sk = -1$ case and is not shown.

3.5. *Production terms*

The primary production term for the $\overline{u'^2}$ Reynolds stress is shown in figure 17. In the smooth-wall case, there is measurable production to the edge of the boundary layer in the ZPG region, but it is suppressed to near zero in the outer half of the boundary layer by station 7, matching the equilibrium DNS. Bader *et al.* (2018) also reported a drop in production for a smooth-wall case along with the frozen turbulence described above. The near-wall peak in figure 17 drops steadily, approaching the level of the DNS by station 7. This is followed by a drop below the DNS, and by station 12 the production is essentially zero everywhere in the boundary layer. This result is consistent with the relaminarisation observed in the mean flow and Reynolds stresses. In the two rough-wall cases, the same drop is observed in the outer region, but in the near-wall region the production appears

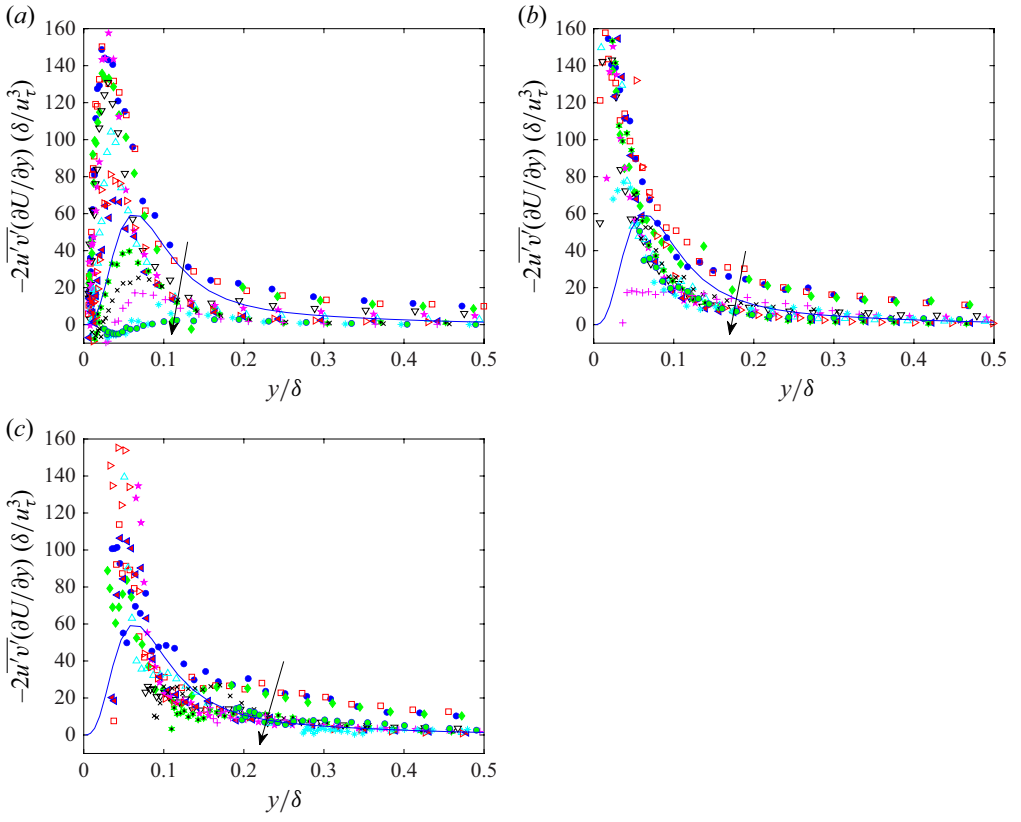

Figure 17. Primary production term for $\overline{u'^2}$: (*a*) smooth wall; (*b*) $Sk = -1$; (*c*) $Sk = +1$. Legend as in figure 8. Arrows indicate progression of profiles in the streamwise direction.

to reach an equilibrium by about station 4. The data lie below the DNS for $y/\delta > 0.06$, but the roughness results in increasing production as the wall is approached, while the smooth-wall DNS shows a drop to zero.

Figure 18 shows the primary production term for $-\overline{u'v'}$. As in figure 17, the production drops steadily in the smooth-wall case, dropping below the equilibrium DNS at 9 for $y/\delta > 0.1$, and to near-zero values at the last station. With the rough wall, there is a rapid drop to an apparent equilibrium when the FPG is imposed. Values in the experiments are just above the equilibrium DNS for $y/\delta > 0.15$, but are several times higher closer to the wall.

3.6. *Higher-order moments*

The higher-order moments of the fluctuating velocity show essentially the same trends as the Reynolds stresses. Two examples that provide additional insight are shown in figures 19 and 20. The skewness of the streamwise component of the velocity, $\overline{u'^3}/(\overline{u'^2})^{3/2}$, is shown in figure 19. The u' skewness is negative across most of the boundary layer, which indicates that strong negative u' motions, which are associated with ejections of low-speed fluid away from the wall, are more significant than strong positive u' motions, which are associated with higher-speed fluid moving towards the wall. In all cases the negative peak located at about $y/\delta = 0.9$ decreases in magnitude in the streamwise direction, suggesting

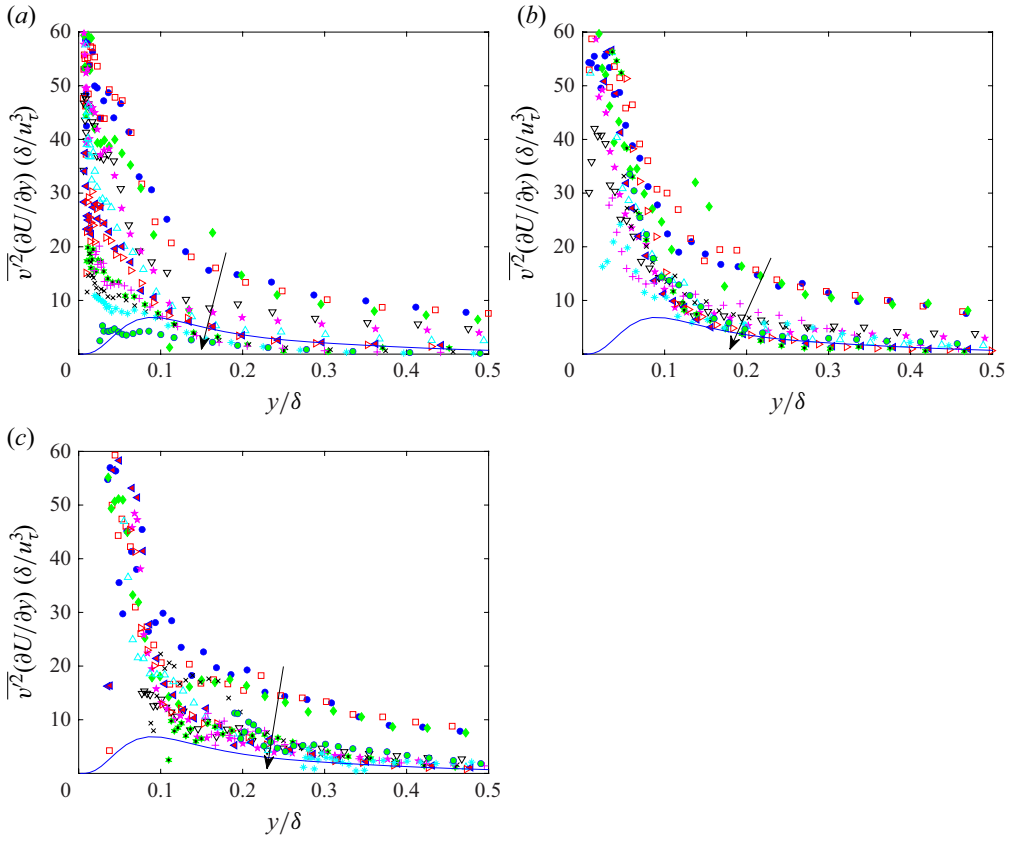

Figure 18. Primary production term for $-\overline{u'v'}$: (*a*) smooth wall; (*b*) $Sk = -1$; (*c*) $Sk = +1$. Legend as in figure 8. Arrows indicate progression of profiles in the streamwise direction.

that the FPG suppresses the larger fluctuations reaching the outer region. In the near-wall region, a second negative peak emerges at the downstream stations. This peak suggests that as the FPG suppresses all of the turbulent fluctuations, the outward motions generated closer to the wall are possibly more persistent. In the smooth-wall case the near-wall peak is confined in the inner half of the boundary layer, while in the rough-wall cases it extends farther out. The v' skewness (not shown) has the same behaviour as the u' skewness, but has positive sign, again associated with motion of low-speed fluid away from the wall.

Figure 20 shows profiles of the kurtosis of the v' fluctuations, $\overline{v'^4}/(\overline{v'^2})^2$. High kurtosis indicates the importance of strong fluctuations relative to the average. Beyond the edge of the boundary layer ($y/\delta > 1$) the FPG suppresses the kurtosis, indicating less of an influence of the strong fluctuations extending into this region in all cases. Near that wall there is an increase at the downstream stations, particularly in the smooth-wall case. As the boundary layer begins to relaminarise in the smooth-wall case, the turbulence level drops, so the occasional stronger fluctuation stands out more and produces a higher kurtosis. There is also some sign of this rise in the rough-wall cases between $y/\delta = 0.5$ and 1, but it less pronounced, possibly because the higher turbulence level in these cases makes the stronger fluctuations less pronounced.

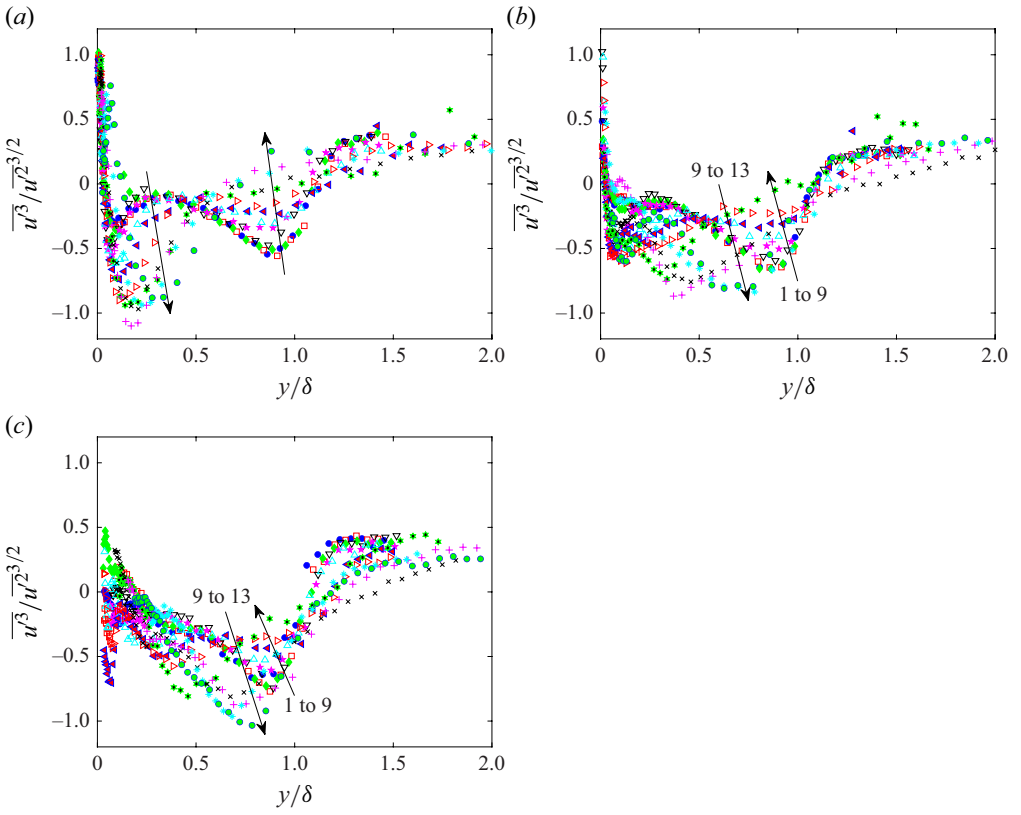

Figure 19. Skewness of u': (*a*) smooth wall; (*b*) $Sk = -1$; (*c*) $Sk = +1$. Legend as in figure 8. Arrows indicate progression of profiles in the streamwise direction.

3.7. *Quadrant analysis*

The boundary layer data were examined using quadrant analysis, as presented by Willmarth & Lu (1972). Quadrants 2 (Q2; ejections, $u' < 0$, $v' > 0$) and 4 (Q4; sweeps, $u' > 0$, $v' < 0$) contribute to negative $\overline{u'v'}$, and are most significant in turbulent boundary layers. Quadrants 1 (Q1; $u' > 0$, $v' > 0$) and 3 (Q3; $u' < 0$, $v' < 0$) have the opposite sign. Examination of the relative contributions from the quadrants can provide insights into the response of the boundary layer to pressure gradients and the behaviour during relaminarisation. Figure 21 shows profiles of the ratio of the combined contributions to $-\overline{u'v'}$ from Q2 and Q4 to the contributions from Q1 and Q3. Under ZPG conditions, for both the smooth- and rough-wall cases, the ratio rises from one at the wall to a peak of about four at $y/\delta = 0.3$. It then drops towards one as the free stream is approached. When the ratio equals one, the turbulent motions are uncorrelated, and the contributions from the four quadrants cancel each other, resulting in zero Reynolds shear stress. On the smooth wall, the peak starts to drop between $y/\delta = 0.2$ and 0.7 at stations 6–8 in response to the FPG. The drop becomes more rapid and extends into the inner region as relaminarisation begins at stations 9–13. The drop in the ratio is consistent with the fluctuating velocities becoming less correlated as the boundary layer becomes more laminar-like. For the $Sk = -1$ case, a similar drop occurs in the centre of the boundary layer at stations 7–9, but the near-wall drop is not observed. It appears that when $k_s{}^+$ is sufficiently small, the

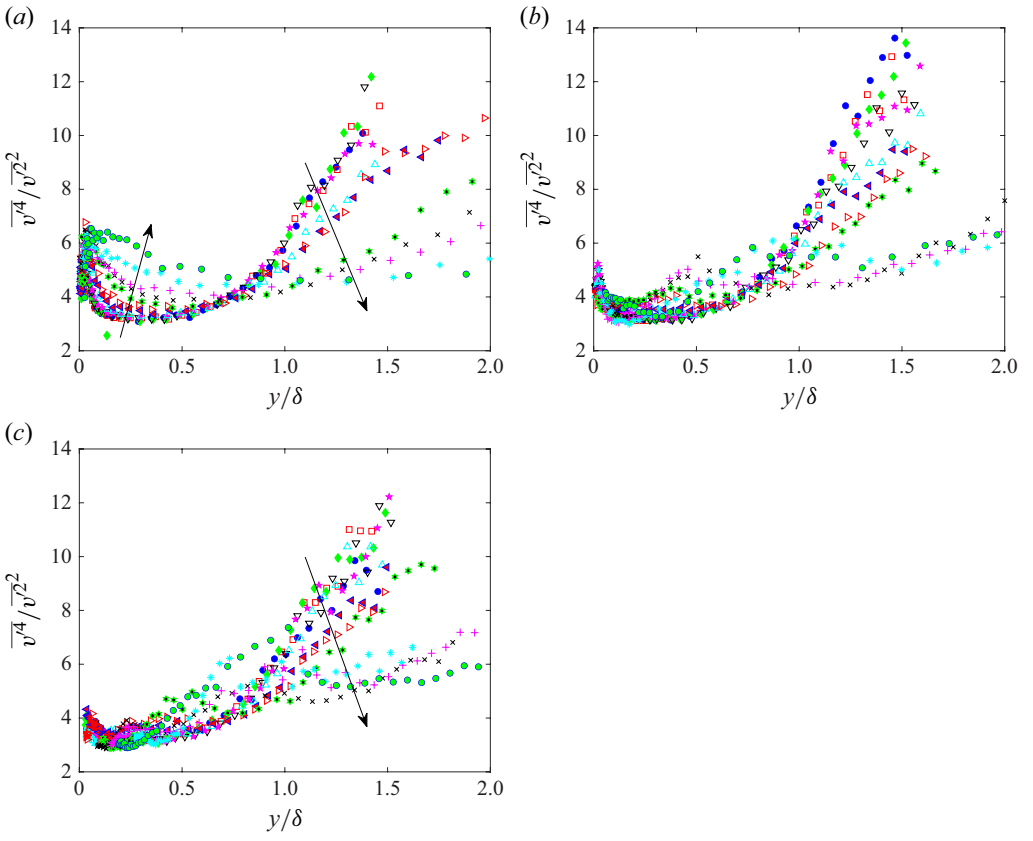

Figure 20. Kurtosis of v': (*a*) smooth wall; (*b*) $Sk = -1$; (*c*) $Sk = +1$. Legend as in figure 8. Arrows indicate progression of profiles in the streamwise direction.

boundary layer begins to respond as in the smooth-wall case, but the roughness sustains the turbulence near the wall. As $k_s{}^+$ rises, the profile returns to the ZPG shape at the downstream stations. For the $Sk = +1$ case, conditions are fully rough, and there is no clear drop in the peak.

Figure 22 shows the ratio of the contributions to $-\overline{u'v'}$ of Q2 and Q4. With a ZPG, in all cases, the ratio rises from the wall to a local peak of about 1.4 at $y/\delta = 0.07$. It then drops to a local minimum of about 1.2 at $y/\delta = 0.3$ before rising to 2 at the edge of the boundary layer. It then drops to one as the turbulence becomes uncorrelated in the free stream. The FPG has a strong effect in suppressing the turbulence in the outer region, which reduces the influence of sweeps moving towards the wall. Ichimiya, Nakamura & Yamashita (1998) also reported changes in sweeps and ejections for a smooth-wall case. In figure 22, this causes the Q2/Q4 ratio to rise in all cases between $y/\delta = 0.1$ and 1 at stations 6–13. Near the wall there is a drop in the ratio at the most downstream stations of the smooth-wall case. As relaminarisation begins, it appears that ejections are suppressed near the wall, causing the Q2/Q4 ratio to drop below ZPG values at stations 11–13. In all cases the Q2/Q4 ratio is also high at the downstream stations for $\delta > 1$. The contribution from all quadrants is small in this region, but it again appears that the FPG is suppressing the sweeps, as in the centre of the boundary layer. The observations appear to be consistent with the quadrant analysis results of Bourassa & Thomas (2009).

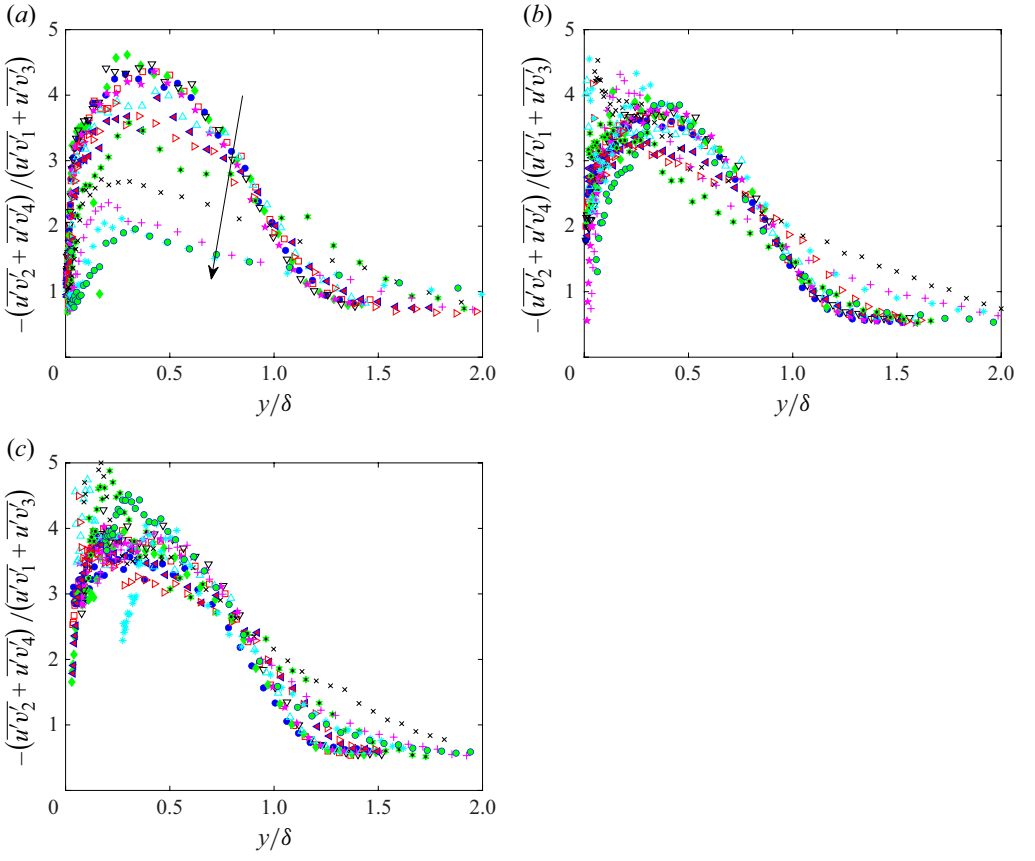

Figure 21. Profiles of ratio of contributions to $\overline{u'v'}$ from (Q2 + Q4) and (Q1 + Q3) with hole size $H = 0$: (*a*) smooth wall; (*b*) $Sk = -1$; (*c*) $Sk = +1$. Legend as in figure 8. Arrow indicates progression of profiles in the streamwise direction.

The hole size, H, can be used to investigate the effect of strong instantaneous fluctuating velocities and is defined such that

$$\overline{u'v'}_i = \frac{\sum_1^N I u'v'_i}{N}, \quad \textit{where } I = \begin{bmatrix} 1 \textit{ if } u'v' \textit{ in quadrant } i \textit{ and } |u'v'| > \left|H\overline{u'v'}\right| \\ 0 \textit{ otherwise}, \end{bmatrix} \tag{3.1}$$

where i is the quadrant number and N is the number of instantaneous samples. When $H = 0$, all the data are used, and the results are as in figures 21 and 22. Figures 23 and 24 show the results of figures 21 and 22 with $H = 5$. Qualitatively the two figures are the same, but with the larger hole size the magnitudes are increased by a factor of about five. The same qualitative behaviour is seen with other hole sizes. The stronger events are more biased towards Q2 and Q4, which is expected since these quadrants are associated with the active motions that promote mixing.

3.8. *Spectra*

To examine the scales of the turbulence, spectra of $-\overline{u'v'}$ are shown in figure 25. Results are shown for $y/\delta = 0.2$, which is near the peak in the $-\overline{u'v'}$ profiles at most stations.

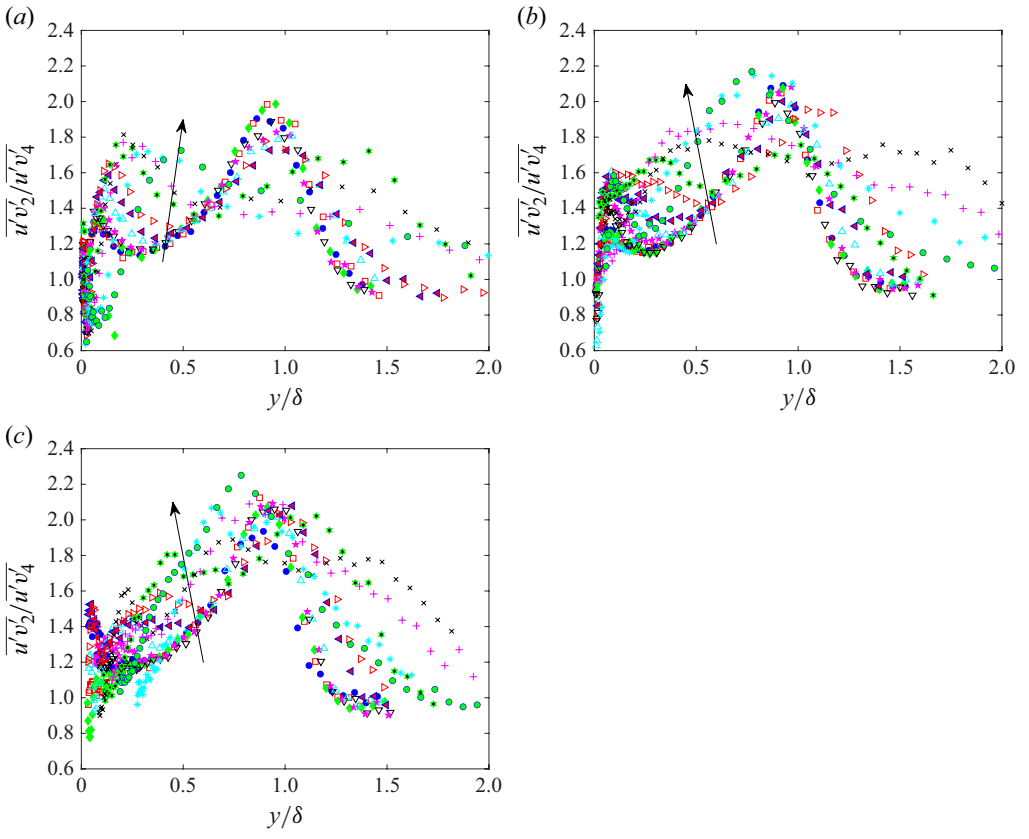

Figure 22. Profiles of ratio of contributions to $\overline{u'v'}$ from Q2 and Q4 with hole size $H = 0$: (*a*) smooth wall; (*b*) $Sk = -1$; (*c*) $Sk = +1$. Legend as in figure 8. Arrows indicate progression of profiles in the streamwise direction.

Frequencies were converted to wavenumber, k, using Taylor's hypothesis with the local mean streamwise velocity. The wavenumbers and premultiplied spectra were normalised using δ and u_τ. In the smooth-wall case, the magnitudes of the spectra drop continuously in the streamwise direction, and the peak moves to lower dimensionless wavenumber. At the most downstream stations, $y/\delta = 0.2$ is in the region where the u' and v' fluctuations are becoming uncorrelated, as shown in figure 21, so the spectral magnitudes drop towards zero. For a different perspective, figure 26 shows the same spectra dimensionally. The smooth-wall case spectra collapse, with peaks at a frequency, f, of about 8 Hz. As noted above, the turbulence in this case is essentially frozen, remaining at the same magnitude as the mean velocity increases.

Spectra for the $Sk = -1$ case are shown in figures 25(*b*) and 26(*b*). Results are similar to the smooth-wall case at stations 1–7. Farther downstream, the relaminarisation seen in the smooth-wall case is not observed. The dimensionless spectra stop changing at stations 7–9, while the dimensional magnitudes and frequencies begin to increase. The turbulence appears to be frozen at first, similar to the smooth-wall case, but eventually the roughness causes the Reynolds shear stress to increase in proportion to the increasing wall shear. The spectra for stations 10–13 are not shown due to limitations of the measurements. The average laser Doppler velocimetry sampling rate was about 180 Hz, which was sufficient to resolve the energy-containing fluctuations through about station 8. At station 9, some

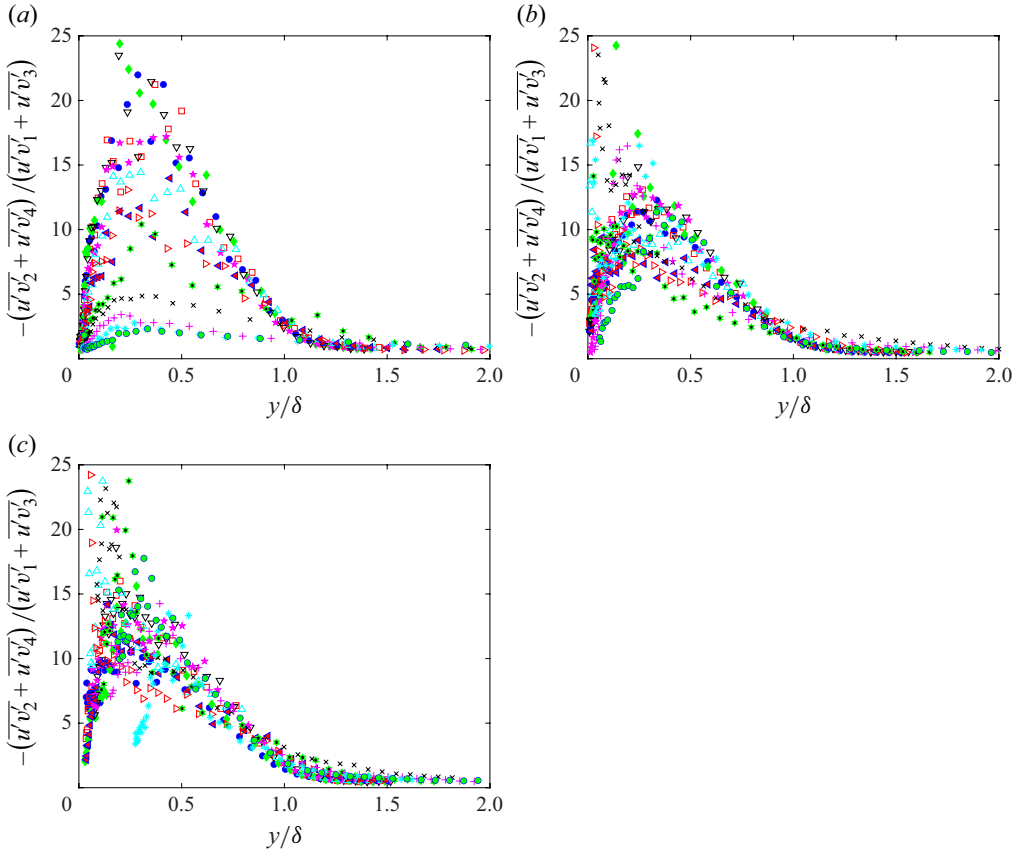

Figure 23. Profiles of ratio of contributions to $\overline{u'v'}$ from (Q2 + Q4) and (Q1 + Q3) with hole size $H = 5$: (*a*) smooth wall; (*b*) $Sk = -1$; (*c*) $Sk = +1$. Legend as in figure 8.

attenuation is clear at the higher frequencies in figure 26(*b*), and farther downstream the attenuation increased, causing aliasing errors.

The $Sk = +1$ case shows a rapid drop of the dimensionless spectra at the beginning of the FPG, and no subsequent change. It appears that a turbulent equilibrium has been reached. The dimensional values show an increase in magnitude and frequency after station 5, similar to the $Sk = -1$ case, but starting farther upstream, presumably due to the larger roughness effect.

4. Conclusions

Boundary layers were subject to strong FPGs with $K = 3.2 \times 10^{-6}$. In all cases the acceleration caused a drop in the turbulence relative to the wall shear, particularly in the outer part of the boundary layer. Sweeps were suppressed relative to ejections originating near the wall. The sink flow boundary layer appeared to approach a turbulent equilibrium, which was similar to that observed in flows with more moderate K. At some locations the mean velocity and turbulence profiles dropped below the lower K equilibrium and then rose towards it from below.

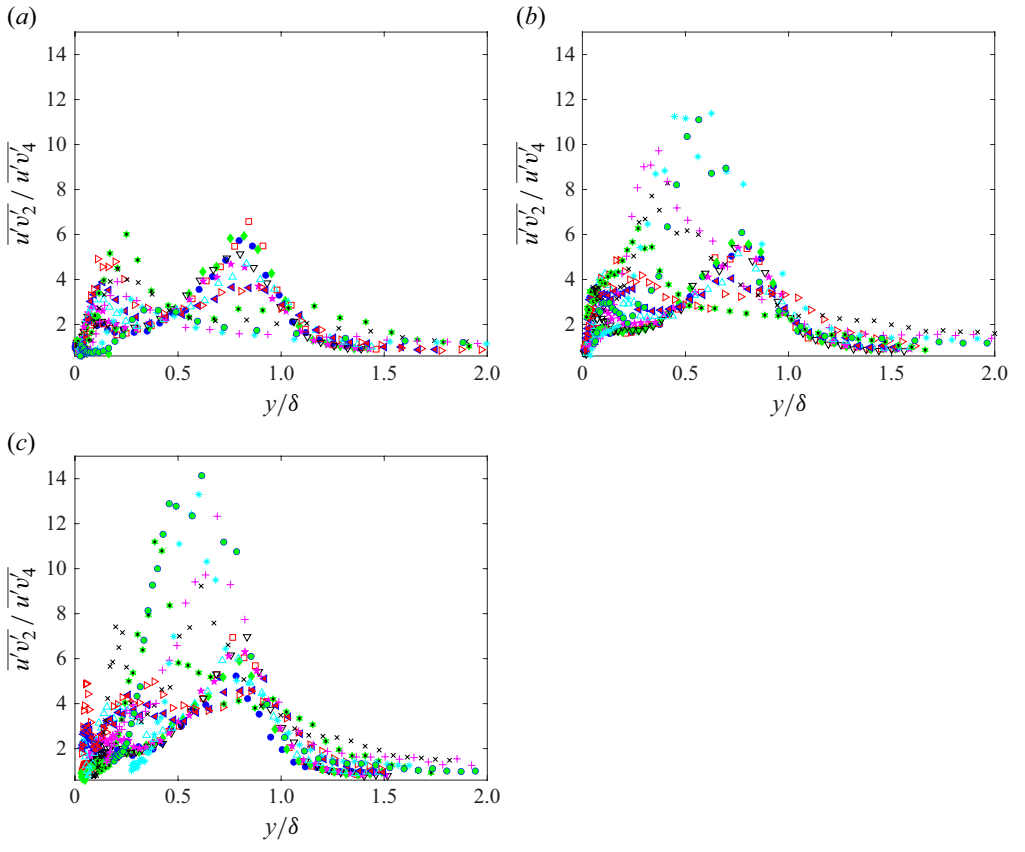

Figure 24. Profiles of ratio of contributions to $\overline{u'v'}$ from Q2 and Q4 with hole size $H = 5$: (*a*) smooth wall; (*b*) $Sk = -1$; (*c*) $Sk = +1$. Legend as in figure 8.

After the initial adjustment to the FPG, the smooth- and rough-wall cases behaved differently. On the smooth wall, after Re_θ had dropped to about 600 in the turbulent boundary layer, relaminarisation began. The turbulence level in the near-wall region dropped, and ejections contributed less relative to sweeps. The fluctuating velocities also lost correlation, causing the Reynolds shear stress to drop more than the normal stresses. In the outer flow the turbulence was essentially frozen, remaining at the values of the upstream ZPG region in both magnitude and frequency instead of rising with U_e and u_τ. The turbulence eventually became insignificant, which resulted in a quasi-laminar boundary layer. The mean velocity profile, shape factor, skin friction coefficient and Reynolds numbers approached those of the analytical laminar sink flow solution.

The rough-wall cases showed no signs of relaminarisation, but the case with the smaller effective roughness did exhibit considerable similarity to the smooth-wall case at the upstream stations. This case had transitionally rough conditions at the upstream stations, with $k_s{}^+ < 20$, and showed some signs of a viscous sublayer. The roughness sustained the turbulence near the wall, and the contribution to $-\overline{u'v'}$ from ejections remained large relative to sweeps, in contrast to the smooth-wall case. The peak in the $-\overline{u'v'}$ spectra remained at a dimensionless wavenumber, $k\delta$, of about 0.3, indicating that smaller-scale

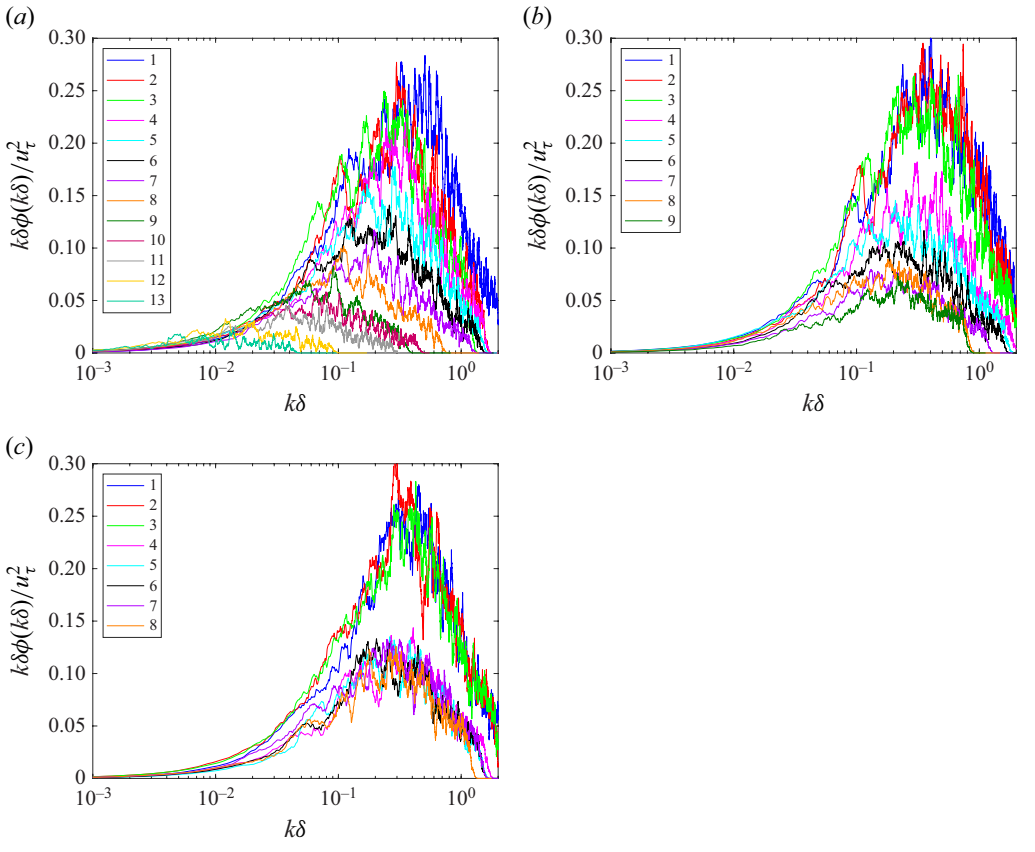

Figure 25. Dimensionless spectra of $-\overline{u'v'}$ at $y/\delta = 0.2$: (*a*) smooth wall; (*b*) $Sk = -1$; (*c*) $Sk = +1$. Legend indicates station number.

eddies were being generated as the velocity increased. The case appeared to have reached a temporary equilibrium.

The case with larger roughness had similar behaviour, but conditions were fully rough, so no signs of a viscous sublayer appeared. At the downstream stations, the profiles were similar to those in the case with smaller roughness, but the Reynolds numbers, shape factor and skin friction coefficient were rising, indicating that this case was not in equilibrium. This was likely due to the drop of δ/k_s to values below five. Since δ decreases continuously in a boundary layer with constant K, any surface with uniform roughness will eventually depart from equilibrium as δ/k_s becomes small. Still, it is interesting that this departure was not large in the present rough-wall cases, even with $\delta/k_s < 10$ in both of them.

Funding. The authors thank the Office of Naval Research for providing financial support under Grant N0001425GI00573, and the United States Naval Academy Hydromechanics Laboratory and Project Support Branch for providing technical support.

Disclaimer. The views expressed in this article are those of the authors and do not reflect the official policy or position of the US Naval Academy, the Department of the Navy, the Department of Defense or the US Government.

Declaration of interests. The authors report no conflict of interest.

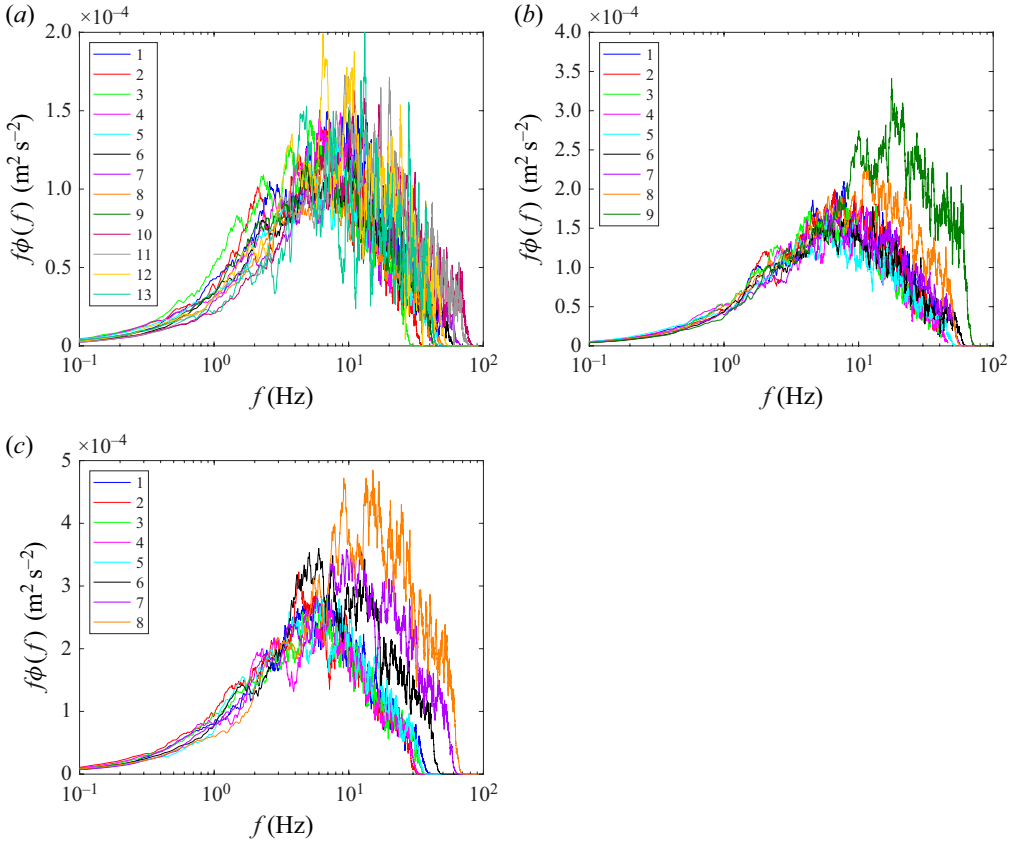

Figure 26. Dimensional spectra of $-\overline{u'v'}$ at $y/\delta = 0.2$: (*a*) smooth wall; (*b*) $Sk = -1$; (*c*) $Sk = +1$. Legend indicates station number.

References

Bader, P., Pschernig, M., Sanz, W., Woisetschläger, J., Heitmeir, F., Meile, W. & Brenn, G. 2018 Experimental investigation of boundary layer relaminarization in accelerated flow. *ASME J. Fluids Engng* **140**, 081201.

Blackwelder, R.F. & Kovasznay, L.S. 1972 Large-scale motion of a turbulent boundary layer during relaminarization. *J. Fluid Mech.* **53**, 61–83.

Bourassa, C. & Thomas, F.O. 2009 An experimental investigation of a highly accelerated turbulent boundary layer. *J. Fluid Mech.* **634**, 359–404.

Bradshaw, P. 1967 Inactive motion and pressure fluctuations in turbulent boundary layers. *J. Fluid Mech.* **30**, 241–258.

Cal, R.B., Brzek, B., Johansson, T.G. & Castillo, L. 2009 The rough favourable pressure gradient turbulent boundary layer. *J. Fluid Mech.* **641**, 129–155.

Cal, R.B. & Castillo, L. 2008 Similarity analysis of favorable pressure gradient turbulent boundary layers with eventual quasilaminarization. *Phys. Fluids* **20**, 105106.

Castillo, L. & George, W.K. 2001 Similarity analysis for turbulent boundary layer with pressure gradient: outer flow. *AIAA J.* **39**, 41–47.

Coleman, H.W., Moffat, R.J. & Kays, W.M. 1977 The accelerated fully rough turbulent boundary layer. *J. Fluid Mech.* **82**, 507–528.

DeGraaff, D.B. 1999 Reynolds number scaling of the turbulent boundary layer on a flat plate and on swept and unswept bumps. *PhD thesis*, Stanford University, USA.

Dixit, S.A. & Ramesh, O.N. 2008 Pressure-gradient-dependent logarithmic laws in sink flow turbulent boundary layers. *J. Fluid Mech.* **615**, 445–475.

ESCUDIER, M.P., ABDEL-HAMEED, A., JOHNSON, M.P. & SUTCLIFFE, C.J. 1998 Laminarisation and re-transition of a turbulent boundary layer subjected to favourable pressure gradient. *Exp. Fluids* **25**, 491–502.
FLACK, K.A., SCHULTZ, M.P. & VOLINO, R.J. 2020 The effect of a systematic change in roughness skewness on turbulence and drag. *Intl J. Heat Fluid Flow* **85**, 108669.
ICHIMIYA, M., NAKAMURA, I. & YAMASHITA, S. 1998 Properties of a relaminarizing turbulent boundary layer under a favorable pressure gradient. *Expl Therm. Fluid Sci.* **17**, 37–48.
JIMÉNEZ, J. 2004 Turbulent boundary layers over rough walls. *Annu. Rev. Fluid Mech.* **36**, 173–196.
JONES, M.B., MARUSIC, I. & PERRY, A.E. 2001 Evolution and structure of sink-flow turbulent boundary layers. *J. Fluid Mech.* **428**, 1–27.
JONES, W.P. & LAUNDER, B.E. 1972 Some properties of sink-flow turbulent boundary layers. *J. Fluid Mech.* **56**, 337–351.
NARASIMHA, R. & SREENIVASAN, K.R. 1973 Relaminarization in highly accelerated turbulent boundary layers. *J. Fluid Mech.* **61**, 417–447.
NARASIMHA, R. & SREENIVASAN, K.R. 1979 Relaminarization of fluid flows. *Adv. Appl. Mech.* **19**, 221–309.
PIOMELLI, U. & YUAN, J. 2013 Numerical simulations of spatially developing, accelerating boundary layers. *Phys. Fluids* **25** (101304), 1–21.
POHLHAUSEN, K. 1921 Zur näherungsweisen integration der differentialgleichung der grenzschict. *Z. Angew. Math. Mech.* **1**, 252–268.
SCHLICHTING, H. 1968 *Boundary-Layer Theory*. 6th edn. McGraw-Hill Book Company.
SPALART, P.R. 1986 Numerical study of sink-flow boundary layers. *J. Fluid Mech.* **172**, 307–328.
SREENIVASEN, K.R. 1982 Laminarescent, relaminarizing, and retransitional flows. *Acta Mechanica* **44**, 1–48.
TACHIE, M.F. & SHAH, M. 2008 Favorable pressure gradient turbulent flow over straight and inclined ribs on both channel walls. *Phys. Fluids* **20** (095103), 1–22.
TOWNSEND, A.A. 1976 *The Structure of Turbulent Shear Flow*. 2nd edn. Cambridge University Press.
VOLINO, R.J. 2020 Non-equilibrium development in turbulent boundary layers with changing pressure gradients. *J. Fluid Mech.* **897**, A2.
VOLINO, R.J. & SCHULTZ, M.P. 2018 Determination of wall shear stress from mean velocity and Reynolds shear stress profiles. *Phys. Rev. Fluids* **3**, 034606.
VOLINO, R.J. & SCHULTZ, M.P. 2022 Effects of boundary layer thickness on the estimation of equivalent sandgrain roughness in zero pressure gradient boundary layers. *Exp. Fluids* **63**, 131.
VOLINO, R.J. & SCHULTZ, M.P. 2023 Comparison of smooth- and rough-wall non-equilibrium boundary layers with favourable and adverse pressure gradients. *J. Fluid Mech.* **959**, A35.
WARNACK, D. & FERNHOLZ, H.H. 1998 The effects of a favourable pressure gradient and of the Reynolds number on an incompressible axisymmetric turbulent boundary layer. Part 2. The boundary layer with relaminarization. *J. Fluid Mech.* **359**, 357–371.
WILLMARTH, W.W. & LU, S.S. 1972 Structure of the Reynolds stress near the wall. *J. Fluid Mech.* **55**, 65–92.
YUAN, J. & PIOMELLI, U. 2014 Numerical simulation of sink-flow boundary layers over rough surfaces. *Phys. Fluids* **26** (015113), 1–28.
YUAN, J. & PIOMELLI, U. 2015 Numerical simulation of spatially developing accelerating boundary layers over roughness. *J. Fluid Mech.* **780**, 192–214.